

Follow-up survey for the binary black hole merger GW200224.222234 using Subaru/HSC and GTC/OSIRIS

TAKAYUKI OHGAMI,¹ JOSEFA BECERRA GONZÁLEZ,^{2,3} NOZOMU TOMINAGA,^{1,4,5,6} TOMOKI MOROKUMA,^{7,8,5}
YOUSUKE UTSUMI,⁹ YUU NIINO,^{8,10} MASAOMI TANAKA,¹¹ SMARANIKA BANERJEE,¹¹ FRÉDÉRIC POIDEVIN,^{2,3}
JOSE ANTONIO ACOSTA-PULIDO,^{2,3} ISMAEL PÉREZ-FOURNON,^{2,3} TEO MUÑOZ-DARIAS,^{2,3} HIROSHI AKITAYA,^{7,12}
KENSUKE YANAGISAWA,^{13,12} MAHITO SASADA,^{12,14} MICHITOSHI YOSHIDA,¹³ MIRKO SIMUNOVIC,¹³ RYOU OHSAWA,^{8,15}
ICHI TANAKA,¹³ TSUYOSHI TERAJ,¹³ YUHEI TAKAGI,¹³ AND THE J-GEM COLLABORATION

¹Division of Science, National Astronomical Observatory of Japan, 2-21-1, Osawa, Mitaka, Tokyo 181-8588, Japan

²Instituto de Astrofísica de Canarias (IAC), E-38200 La Laguna, Tenerife, Spain

³Universidad de La Laguna (ULL), Departamento de Astrofísica, E-38206 La Laguna, Tenerife, Spain

⁴Department of Astronomical Science, School of Physical Sciences, The Graduate University of Advanced Studies, (SOKENDAI), 2-21-1 Osawa, Mitaka, Tokyo 181-8588, Japan

⁵Kavli Institute for the Physics and Mathematics of the Universe (WPI), The University of Tokyo, 5-1-5 Kashiwanoha, Kashiwa, Chiba 277-8583, Japan

⁶Department of Physics, Faculty of Science and Engineering, Konan University, 8-9-1 Okamoto, Kobe, Hyogo 658-8501, Japan

⁷Planetary Exploration Research Center, Chiba Institute of Technology, 2-17-1 Tsudanuma, Narashino, Chiba 275-0016, Japan

⁸Institute of Astronomy, Graduate School of Science, The University of Tokyo, 2-21-1 Osawa, Mitaka, Tokyo 181-0015, Japan

⁹Kavli Institute for Particle Astrophysics and Cosmology (KIPAC), SLAC National Accelerator Laboratory, Stanford University, 2575 Sand Hill Road, Menlo Park, CA 94025, USA

¹⁰Research Center for the Early Universe, Graduate School of Science, The University of Tokyo, 7-3-1 Hongo, Bunkyo-ku, Tokyo 113-0033, Japan

¹¹Astronomical Institute, Tohoku University, Sendai, Miyagi 980-8578, Japan

¹²Hiroshima Astrophysical Science Center, Hiroshima University, 1-3-1 Kagamiyama, Higashi-Hiroshima, Hiroshima 739-8526, Japan

¹³Subaru Telescope, National Astronomical Observatory of Japan, 650 North A'ohoku Place, Hilo, HI 96720, USA

¹⁴Mizusawa VLBI Observatory, National Astronomical Observatory of Japan, 2-12 Hoshigaoka, Mizusawa, Oshu, Iwate 023-0861, Japan

¹⁵JASMINE Project, National Astronomical Observatory of Japan, 2-21-1, Osawa, Mitaka, Tokyo 181-8588, Japan

ABSTRACT

The LIGO/Virgo detected a gravitational wave (GW) event, named GW200224.222234 (a.k.a. S200224ca) and classified as a binary-black-hole coalescence, on February 24, 2020. Given its relatively small localization skymap (71 deg² for a 90% credible region; revised to 50 deg² in GWTC-3), we performed target-of-opportunity observations using the Subaru/Hyper Suprime-Cam (HSC) in the r - and z -bands. Observations were conducted on February 25 and 28 and March 23, 2020, with the first epoch beginning 12.3 h after the GW detection. The survey covered the highest probability sky area of 56.6 deg², corresponding to a 91% probability. This was the first deep follow-up ($m_r \gtrsim 24$, $m_z \gtrsim 23$) for a binary-black-hole merger covering >90% of the localization. By performing image subtraction and candidate screening including light curve fitting with transient templates and examples, we found 22 off-nucleus transients that were not ruled out as the counterparts of GW200224.222234 with only our Subaru/HSC data. We also performed GTC/OSIRIS spectroscopy of the probable host galaxies for five candidates; two are likely to be located within the 3D skymap, whereas the others are not. In conclusion, 19 transients remain as possible optical counterparts of GW200224.222234; however, we could not identify a unique promising counterpart. If there are no counterparts in the remaining candidates, the upper limits of optical luminosity are $\nu L_\nu < 5.2^{+2.4}_{-1.9} \times 10^{41}$ erg s⁻¹ and $\nu L_\nu < 1.8^{+0.8}_{-0.6} \times 10^{42}$ erg s⁻¹

Corresponding author: Takayuki Ohgami
takayuki.ohgami@nao.ac.jp

Corresponding author: Josefa Becerra González
jbecerra@iac.es

Corresponding author: Nozomu Tominaga
nozomu.tominaga@nao.ac.jp

in the r - and z -bands, respectively, at ~ 12 h after GW detection. We also discuss improvements in the strategies of optical follow-ups for future GW events.

Keywords: Gravitational waves (678); Black holes (162); Surveys (1671)

1. INTRODUCTION

In general relativity, massive objects radiate energy via the distortion of space time when their motion is accelerated. This energy radiation predicted by Einstein is called a gravitational wave (GW; [Einstein 1916, 1918](#)). Astronomical objects or phenomena are expected to be sources of GW signals with a large amplitude, which may be detected by current instruments. For example, binary systems composed of compact objects such as black holes (BHs) or neutron stars (NSs) emit strong GWs at their coalescence.

In the second observation run of the GW interferometers LIGO and Virgo, they detected a GW signal from a binary-NS (BNS) coalescence using three detectors, and the localization area was constrained to 28 deg^2 for a 90% credible region (GW170817; [Abbott et al. 2017](#)). The electromagnetic (EM) counterpart of GW events was observed for the first time by multiple observatories across the EM spectrum from radio to γ -rays ([Andreoni et al. 2017](#); [Arcavi et al. 2017](#); [Chornock et al. 2017](#); [Coulter et al. 2017](#); [Cowperthwaite et al. 2017](#); [Díaz et al. 2017](#); [Drout et al. 2017](#); [Evans et al. 2017](#); [Kasliwal et al. 2017](#); [Lipunov et al. 2017](#); [Nicholl et al. 2017](#); [Pian et al. 2017](#); [Smartt et al. 2017](#); [Soares-Santos et al. 2017](#); [Troja et al. 2017](#); [Tanvir et al. 2017](#); [Tominaga et al. 2018a](#); [Utsumi et al. 2017](#); [Valenti et al. 2017](#)). It was demonstrated that BNS mergers are accompanied by explosive EM emissions called kilonova (e.g., [Kasen et al. 2013](#); [Shibata et al. 2017](#); [Tanaka et al. 2017](#); [Kawaguchi et al. 2018](#); [Perego et al. 2017](#); [Rosswog et al. 2018](#); [Banerjee et al. 2020](#)).

In contrast to NS mergers, binary-BH (BBH) mergers are not considered to be accompanied by any EM emission. However, the Fermi Gamma-ray Burst Monitor (GBM) reported the presence of a weak γ -ray transient after the detection of GW150914 ([Connaughton et al. 2016](#)). Although the physical association between GWs and γ -ray signals is ambiguous, and it is unclear whether the γ -ray signal is truly astronomical because of the low flux, various scenarios have been proposed, such as BBHs surrounded by pre-existing material, for example, a circumbinary disc ([Martin et al. 2018](#)), an accretion disc surrounding a galactic center BH ([Bartos et al. 2017](#)), and remnants

of gravitational collapse ([Janiuk et al. 2017](#)). Another case is the detection of an optical counterpart candidate of GW190521 by the Zwicky Transient Facility (ZTF19abahr). [Graham et al. \(2020\)](#) suggested that the EM flare is consistent with the behavior expected from a kicked BBH merger in an accretion disk of an active galactic nucleus (AGN, [McKernan et al. 2019](#)) and ruled out other scenarios (for example, the intrinsic variability of AGN, supernova, microlens, tidal disruption). [Graham et al. \(2022\)](#) comprehensively searched for EM counterparts to BBH mergers and identified nine candidates. To test various scenarios for EM radiation from a BBH merger, it is still important to perform follow-ups of the BBH mergers.

The LIGO/Virgo collaboration began their third observation run (O3) in April 2019 and detected a GW event named GW200224_222234 (a.k.a. S200224ca) using three detectors on February 24, 2020 at 22:22 UTC ([The LIGO Scientific Collaboration et al. 2021](#); [LIGO Scientific Collaboration & Virgo Collaboration 2020](#)). They released a preliminary localization skymap derived using software called BAYESTAR ([Singer & Price 2016](#)) on February 24, 2020 at 22:32 UTC. In this release, the GW event was classified as a BBH coalescence with a $> 99\%$ confidence level and a false alarm rate of $1.6 \times 10^{-11} \text{ Hz}$ (approximately one in 1975 years). The luminosity distance was $1583 \pm 331 \text{ Mpc}$, corresponding to a redshift of 0.30 ± 0.05 , and the 90% localization sky area was as narrow as 71 deg^2 .

Upon receiving the alert for GW200224_222234, the Japanese collaboration for Gravitational wave ElectroMagnetic follow-up (J-GEM; [Morokuma et al. 2016](#); [Utsumi et al. 2017](#); [Sasada et al. 2021](#)) triggered a target-of-opportunity (ToO) observation to search for its EM counterpart on February 25, 2020 at 10:43 UTC ([Ohgami et al. 2020](#)) using Hyper Suprime-Cam (HSC; [Furusawa et al. 2018](#); [Kawanomoto et al. 2018](#); [Komiya et al. 2018](#); [Miyazaki et al. 2012, 2018](#)), which is a wide-field imager installed on the prime focus of the Subaru Telescope. Its field of view (FoV) of 1.77 deg^2 is the largest among current 8 m-class telescopes, which makes the Subaru/HSC the most efficient instrument for the optical survey. The first exposure commenced at approximately 12.3 h after GW detection, and the observation area reached 56.6 deg^2 . We also

conducted additional ToO observations using the Subaru/HSC on February 28 and March 23, 2020, in the same fields as the first epoch observation. The LIGO and Virgo collaboration published the GWTC-3 catalog (The LIGO Scientific Collaboration et al. 2021) including the observations O1, O2, O3a, and O3b and also released the reanalyzed the localization skymap. The 90% localization sky area was updated from 71 deg^2 to 50 deg^2 . Our observation area corresponds to a cumulative probability of 91% in the updated skymap.

In this paper, we describe the details of the follow-ups of GW200224_222234 using the Subaru/HSC, the candidate selection algorithm, and a list of candidates, including spectroscopic observations of the probable host galaxies of the five candidates to measure their spectroscopic redshifts using the Optical System for Imaging and low-Intermediate-Resolution Integrated Spectroscopy¹ (OSIRIS), which is an imager and spectrograph for the optical wavelength range, installed in the 10.4-m Gran Telescopio CANARIAS (GTC). All magnitudes are given in AB magnitudes.

2. OBSERVATIONS WITH THE SUBARU/HSC AND DATA ANALYSIS

2.1. ToO observation

We conducted optical imaging observations using the Subaru/HSC on February 25 (Day 1), 28 (Day 4), and March 23 (Day 28), 2020, in the $r2$ - and z -bands. To trigger our ToO follow-up as rapidly as possible, we conducted the first observations in the $r2$ -band, which had already been set in the Subaru/HSC at the time of the GW alert. The first exposure commenced on February 25, 2020 at 10:43 UTC, corresponding to 12.3 h after GW detection. We selected 60 observation pointings to cover the high probability area in the BAYSTAR skymap for the HEALPix grid with a resolution of $\text{NSIDE} = 64$, which corresponds to $0.84 \text{ deg}^2 \text{ pixel}^{-2}$, enabling overlap of the FoVs. Figure 1 shows the survey pointing map. Our survey area covered 56.6 deg^2 , corresponding to a cumulative probability of 91% in the localization skymap refined in the GWTC-3 catalog using the IMRPhenomXPHM model (Pratten et al. 2021), which models higher-order spherical harmonics and spin precession. In this study, we used the localization skymap created using the IMRPhenomXPHM model as the 3D localization of GW200224_222234.

On February 25 and 28, 2020, we observed these pointings with 30 s of exposure each in pointing ID order and revisited them in each band. The revisits were con-

ducted at least 1 h apart with a $1'$ offset in each pointing to fill the CCD gaps. Note that some areas were observed again at a time interval of less than 1 h because of the overlap between each pointing. On March 23, 2020, we changed the exposure time and the order of the pointings. The pointings at higher elevation were observed earlier. In the z -band, we took the shots with a 35-s exposure each and revisited them. In the $r2$ -band, we took the shots with 50-s exposures for the first 32 pointings and 70-s exposures for the remaining 28 pointings. The central coordinates and exposure times are shown in Table 1 (This table is published in its entirety in the machine-readable format).

2.2. Data reduction and image subtraction

We reduced the observational data using *hscPipe* v4.0.5 (Bosch et al. 2018), which is a standard analysis pipeline for the HSC. This pipeline provides full packages for data analyses, which include image subtraction and source detection. We evaluated the limiting magnitudes of the stacked images in each epoch as follows: We assumed an aperture with a diameter of twice the full width at half maximum (FWHM) of the point spread function (PSF) and distributed it randomly, avoiding existing sources. Measuring the 5σ deviations of fluxes in this aperture, we obtained a map of the 5σ limiting magnitudes for each stack image. Table 2 lists the mode², maximum, and minimum values of the 5σ limiting magnitudes. The 5σ limiting magnitudes scattered with a range of $\sim 1 \text{ mag}$, and there were differences of approximately 1 mag between those of the $r2$ - and z -bands. Note that the limiting magnitudes in the $r2$ -band on March 23, 2020, had a small positional dependence owing to the different exposure time.

We performed image subtraction for the science images obtained in the first (one day from GW detection; Day 1) and second (Day 4) epochs using the images taken in the third (Day 28) epoch as reference images. The subtraction package is included in *hscPipe* v4.0.5 and is based on an algorithm in which the FWHM of the reference images is fitted to that in the science images via convolution using kernels to make their PSFs equivalent, as proposed in Alard & Lupton (1998) and Alard (1999). Table 3 lists the mode, maximum, and minimum values of the 5σ limiting magnitudes evaluated from the

¹ <http://www.gtc.iac.es/instruments/osiris/>

² The mode values are the peak values of the histograms of the 5σ limiting magnitudes. Here, we distributed the 5σ limiting magnitudes into ten bins ranging between the maximum and minimum values.

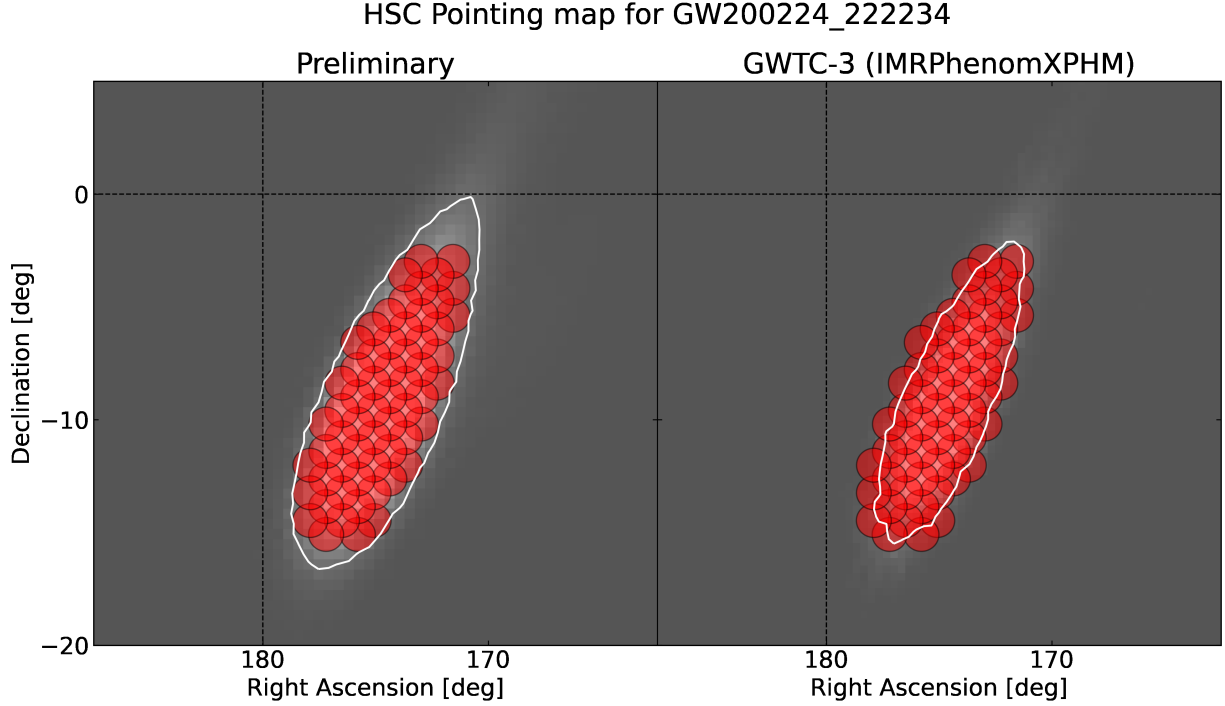


Figure 1. Observation pointings with the Subaru/HSC (red filled circles). The left and right panels are the preliminary localization sky map of GW200224_222234 (BAYESTAR; [LIGO Scientific Collaboration & Virgo Collaboration 2020](#)) and a refined version using the IMRPhenomXPHM model (GWTC-3 catalog; [The LIGO Scientific Collaboration et al. 2021](#)), respectively. The white contour lines indicate the 90% credible regions.

Table 1. Central coordinates and exposure times of the observation pointings with the Subaru/HSC.

Pointing ID	Central Coordinate		Exposure Time					
	R.A. (J2000.0) (HH:MM:SS.ss)	Decl. (J2000.0) (DD:MM:SS.s)	2020-02-25 (Day 1)		2020-02-28 (Day 4)		2020-03-23 (Day 28)	
			$r2$	z	$r2$	z	$r2$	z
00	11:40:18.75	−14:28:39.0	30 s×2	30 s×2	30 s×2	30 s×2	50 s	35 s×2
01	11:34:41.25	−12:01:28.9	30 s×2	30 s×2	30 s×2	30 s×2	70 s	35 s×2
02	11:31:52.50	−10:11:59.7	30 s×2	30 s×2	30 s×2	30 s×2	50 s	35 s×2
03	11:43:07.50	−15:05:41.2	30 s×2	30 s×2	30 s×2	30 s×2	70 s	35 s×2
04	11:37:30.00	−12:38:08.3	30 s×2	30 s×2	30 s×2	30 s×2	70 s	35 s×2
⋮	⋮	⋮	⋮	⋮	⋮	⋮	⋮	⋮

NOTE—This table is published in its entirety in the machine-readable format. A portion is shown here for guidance regarding its form and content.

difference images. The positional dependence of the 5σ limiting magnitudes in the $r2$ -band is shown in Figure 2.

2.3. Source detection and screening

After image subtraction, we applied the following criteria to exclude bogus detections (for example, caused

by bad pixels and failure of image subtraction) and select point sources from the difference images as in [Tominaga et al. \(2018a\)](#) and [Ohgami et al. \(2021\)](#): (i) A signal-to-noise ratio of PSF flux $(S/N)_{\text{PSF}} > 5$; (ii) $(b/a)/(b/a)_{\text{PSF}} > 0.65$, where a and b are the lengths of the major and minor axes, respectively, of the shape of a source; (iii) $0.7 < \text{FWHM}/(\text{FWHM})_{\text{PSF}} < 1.3$; (iv)

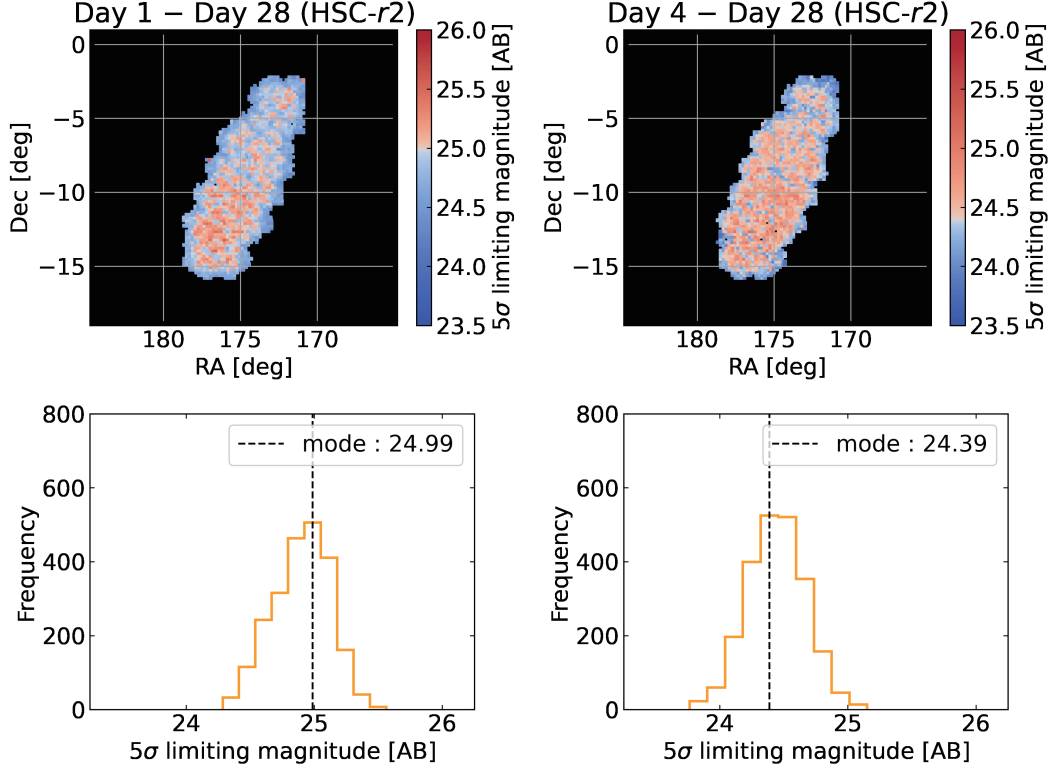


Figure 2. Map (top) and histogram (bottom) of the 5σ limiting magnitudes in the difference images within the first (Day 1 – Day 28; left) and second epochs (Day 4 – Day 28; right) in the $r2$ -band. The color indicates larger/smaller (in red/blue) values than the mode value of each epoch.

Table 2. Mode, maximum, and minimum values of the 5σ limiting magnitudes in the stacked images.

Date (Days from GW detection)	Filter	Limiting magnitude (AB)		
		mode	max	min
2020-02-25 (Day 1)	$r2$	25.29	25.71	24.51
	z	23.56	24.14	22.84
2020-02-28 (Day 4)	$r2$	24.61	25.13	23.98
	z	23.21	23.76	22.54
2020-03-23 (Day 28)	$r2$	25.53	26.25	24.64
	z	23.83	24.64	22.85

PSF-subtracted residual with $< 3\sigma$ standard deviation in the difference image. Furthermore, we imposed the following criterion to exclude moving objects such as minor planets: (v) Detection at least twice in the difference images. As a result, we obtained 5213 variable point sources. To evaluate the completeness of transient detection with image subtraction and our detection criteria, we randomly injected artificial point sources with various magnitudes into the observed images and detected them in the difference images using the same detection

Table 3. Mode, maximum, and minimum values of the 5σ limiting magnitudes in the difference images.

Difference Image	Filter	Limiting magnitude (AB)		
		mode	max	min
Day 1–28	$r2$	24.99	25.56	24.29
	z	23.28	23.89	22.54
Day 4–28	$r2$	24.39	25.15	23.76
	z	22.97	23.57	22.23

criteria. Figure 3 shows the completeness of transient detection in the difference images within the first (top: Day 1–28) and second epochs (bottom: Day 4–28). The vertical dotted lines indicate the mode values of the 5σ limiting magnitudes, and these magnitudes were approximately comparable to the magnitude for a completeness of 23% (Day 1–28, r), 29% (Day 1–28, z), 39% (Day 4–28, r), and 32% (Day 4–28, z).

Figure 4 shows a flowchart of the candidate screening and classification process for the detected sources. We first checked whether the sources were associated with known objects (for example, variable stars and AGNs)

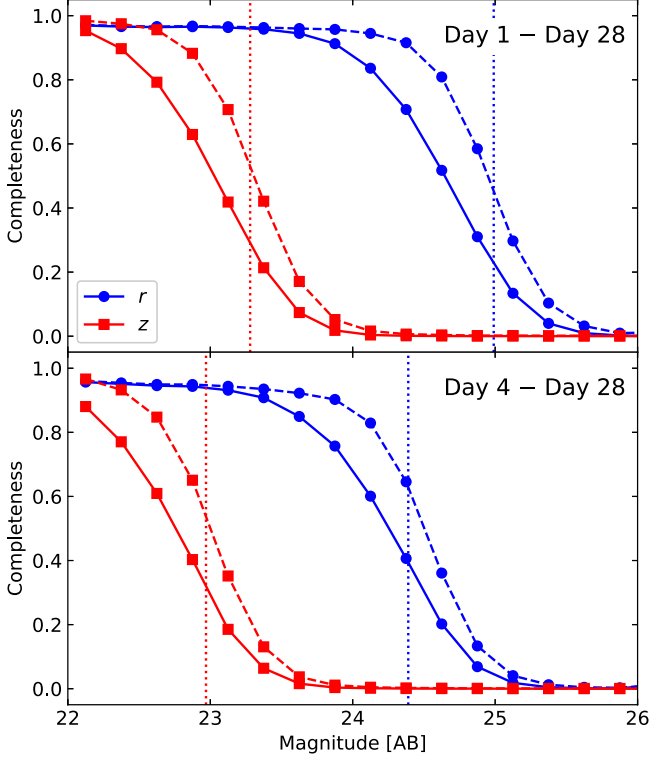


Figure 3. Completeness of transient detection in the difference images (top: Day 1–28; bottom: Day 4–28). The dashed curves are the detection fractions of artificial point sources as a function of magnitude. The solid curves are the detection fractions of the remaining artificial point sources after applying Criteria (i)–(iv). The vertical dotted lines indicate the mode values of the 5σ limiting magnitudes.

by matching these sources with the Pan-STARRS1 (PS1) catalog (Flewelling et al. 2020) within $1''$. Furthermore, to classify the PS1 objects, we used a flag, `objInfoFlag`, that indicates if an object is extended or not. As a result, we found that 2743 and 1883 sources were associated with stellar-like objects and extended objects, respectively. The former are likely to have originated from stellar variabilities, and thus we excluded them as candidates of an EM counterpart of GW200224_222234. The latter could be variabilities of AGNs, an EM signal from a BBH coalescence, or something else. The rate of BBH coalescence may be enhanced in galactic nuclei (for example, McKernan et al. 2019; Tagawa et al. 2020a,b). The light curves of AGNs are stochastic (for example, Vanden Berk et al. 2004), and thus a clear difference between AGN variability and a catastrophic phenomenon such as BBH coalescence is the long-term variability. However, it was not possible to distinguish them from only our three-nights’ observation over one month. Therefore, we also excluded the 1883 sources associated with extended objects in this study.

Further examination is left to future studies. After this selection, 587 sources remained in the sample.

As the next step, we performed a visual inspection to exclude bogus detections and obtained 223 plausible candidates. Then, we classified these candidates by whether there are extended objects in the PS1 catalog within an angular separation, θ_{sep} . Here, we classified them into two groups: “off-center” candidates ($1'' \leq \theta_{\text{sep}} \leq 15''$) and “hostless” candidates ($\theta_{\text{sep}} > 15''$). We conservatively adopted the threshold ($\theta_{\text{sep}} = 15''$) corresponding to a separation of ~ 60 kpc at the distance of GW200224_222234 ($z \sim 0.3$). This separation is larger than the typical size of galaxies (for example, Shen et al. 2003; Kauffmann et al. 2003). Then, we investigated off-center candidates with large separation individually. As a result, we obtained 118 off-center candidates and 105 hostless candidates.

Furthermore, we calculated the probability P_{3D} for 118 off-center candidates. P_{3D} represents how likely the extended objects were to be located inside the 3D skymap of GW200224_222234. The definition and calculation method are described in Tominaga et al. (2018a). We used the r - and/or i -band Kron-magnitudes (`rMeanKronMag`, `iMeanKronMag` in the PS1 catalog) of the extended objects to derive the absolute magnitudes of probable host galaxy in the observer frame. We classified them with a threshold of $P_{3D} = 0.5$ and obtained 93 likely candidates within the 3σ error of the arrival distance of GW200224_222234 ($P_{3D} \geq 0.5$) and 16 candidates that were likely outside ($P_{3D} < 0.5$). The remaining nine candidates had no information of the Kron-magnitudes in the r - and i -bands in the PS1 catalog (`rMeanKronMag` = `iMeanKronMag` = -999) and were classified as “No Info.” In the following, we investigate the nature of 93 candidates inside the 3D skymap, 16 candidates outside the 3D skymap, nine candidates without host galaxy information, and 105 hostless candidates.

3. LIGHT CURVE FITTING

3.1. Method

We performed light curve fitting using transient templates and examples to exclude common transients such as supernovae (SNe) from the 223 candidates. We adopted a template set including the transient templates of Type Ia SNe (Hsiao et al. 2007) and core-collapse SNe (CCSNe; Type Ibc, IIP, IIL, and IIn, Nugent et al. 2002), and examples of rapid transients (RTs, Drout et al. 2014) as in Tominaga et al. (2018b). RTs were included in the template set despite their low rate (Drout et al. 2014) because their nature is still under debate and they could have a similar timescale

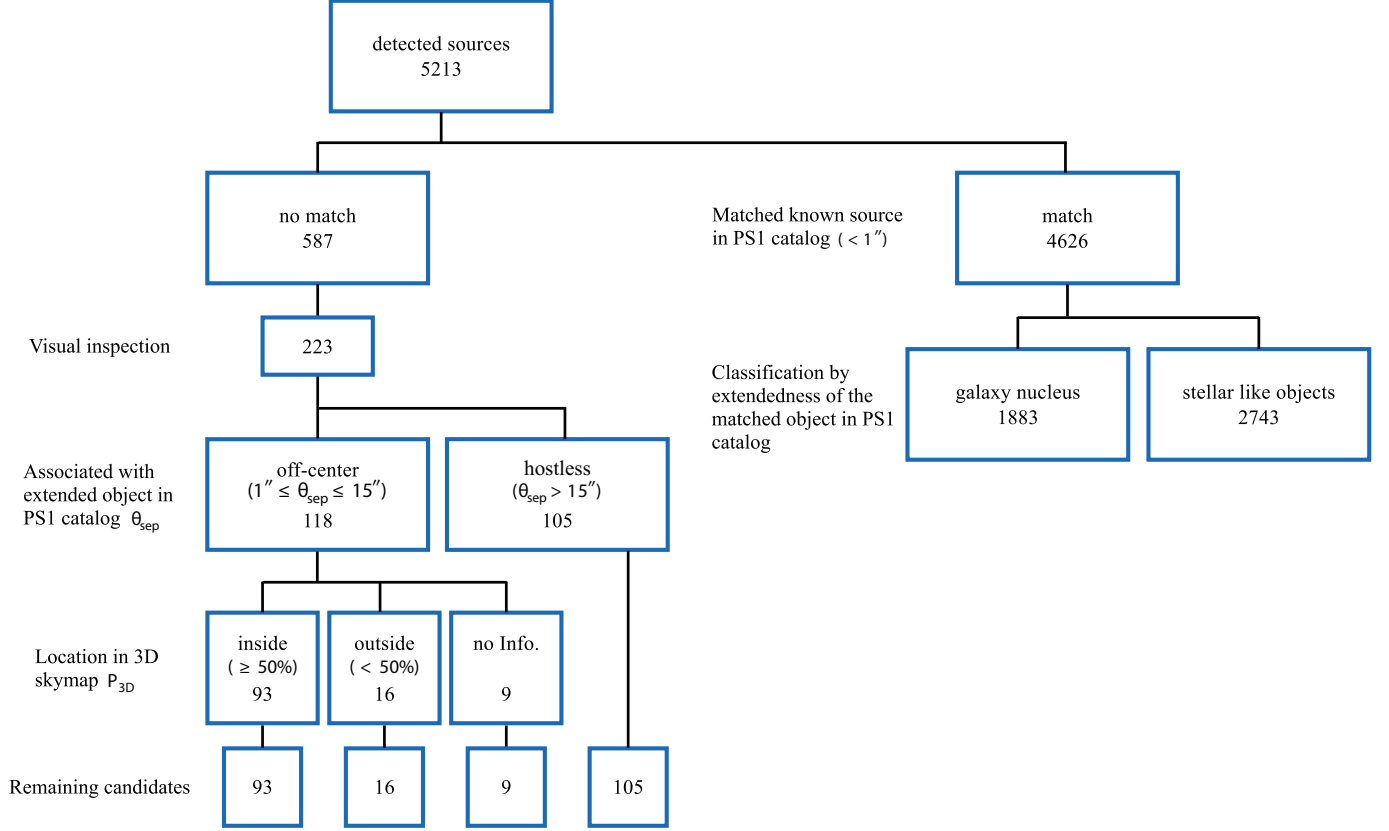


Figure 4. Flowchart of the candidate screening and classification process for the detected sources after image subtraction. The number in each box represents the number of remaining sources after each process.

to a possible EM counterpart of BBH coalescence (McKernan et al. 2019). The template set did not include other types of transients, such as superluminous SNe (Inserra et al. 2021) and SNe amplified by a gravitational lens (Oguri & Marshall 2010), because there is no indication that they are associated with BBH coalescence, and their rates are sufficiently low that no detection was expected in our observation (for example, Quimby et al. 2014; Moriya et al. 2019). Note that the probability that the nature of detected candidates is that of such transients cannot be excluded.

We derived the light curves of 223 candidates via forced PSF photometry of the difference images at their location. The difference fluxes of the candidates were measured using the difference images with the local background subtracted. Note that the difference fluxes could not be the genuine fluxes of candidates because the time interval between the science and reference images was shorter than the typical timescales of SNe. Thus, forced PSF photometry was also performed for the stacked images without the local background subtracted. The measured fluxes included the fluxes of their host galaxies as well as the genuine fluxes of candidates and thus were adopted as the upper limits of the gen-

uine fluxes of candidates. Then, we performed template fitting not only to the difference fluxes but also to the upper limits.

We considered a variation in the explosion date and an intrinsic variation in templates and examples. The light curve templates were derived with an explosion date t_{exp} , redshift z , and variations as conducted in Tominaga et al. (2018b). To account for the variations in supernova properties, we derived the peak absolute B -band magnitude M_B using Equation (4) in Barbary et al. (2012) by considering the stretch s , color c , and intrinsic variation I for the template of a Type Ia SN. For CCSNe and RTs, we parameterized M_B and the color excess of their host galaxy E_{B-V} characterizing the extinction of the host galaxy. We assumed that the extinction curve of the host galaxy was the same as that in our Galaxy (Pei 1992).

To evaluate the difference between the observed light curves and the template, we defined the following ξ value:

$$\xi := \sum_i^{N_d^{obs}} \frac{(f_{d,i}^{obs} - f_{d,i}^{temp}(p))^2}{\sigma_{d,i}^{obs2}}$$

$$+ \sum_j^{N_s^{\text{obs}}} \frac{(f_{s,j}^{\text{obs}} - f_{s,j}^{\text{temp}}(p))^2}{\sigma_{s,j}^{\text{obs}^2}}, \quad (1)$$

where the subscripts d and s indicate quantities derived from the difference images (d) and stacked images (s), respectively, N_s^{obs} is the number of data points of the observation, f_s^{obs} and σ_s^{obs} are the observed flux and its error, respectively, and $f^{\text{temp}}(p)$ is the template flux calculated using a template parameter set p . When $f_{s,j}^{\text{obs}} - f_{s,j}^{\text{temp}} > 0$, we set $\sigma_{s,j}^{\text{obs}}$ to infinity because the flux in the stacked image is an upper limit of the genuine flux of the candidate.

The 5σ limiting magnitudes in the difference images correspond to $0.37 \mu\text{Jy}$ (Day 1–28) and $0.64 \mu\text{Jy}$ (Day 4–28) in the r -band flux, and $1.77 \mu\text{Jy}$ (Day 1–28) and $2.36 \mu\text{Jy}$ (Day 4–28) in the z -band flux. Most of these candidates were detected in the r -band but not in the z -band. If the difference flux was lower than the flux corresponding to the 5σ limiting magnitudes, we required the template flux to be fainter than the flux corresponding to the 5σ limiting magnitudes.

We applied the Metropolis–Hastings (MH) algorithm, which is a type of Markov-chain Monte Carlo (MCMC) method, for the template fitting. This method can derive best-fit template parameter sets without being trapped by the local minima of ξ by probabilistically moving to a location where ξ is smaller in a parameter space. We applied the top-hat function as a prior probability distribution with the same parameter ranges as adopted in Tominaga et al. (2018b). The ranges were obtained from Barbary et al. (2012) for the Type Ia SN, Dahlen et al. (2012) for CCSNe, and an assumption of ± 1 mag variation for RTs, as shown in Table 4. We derived a Markov chain using 50000 samples with each redshift from 0.00 to 0.50 every 0.05 using each template model (Type Ia SN, 6 CCSNe, and 9 RTs). Each sample of the Markov chain was proposed from a Gaussian distribution with the standard deviation shown in Table 4, using the current value as the median. The initial values of each parameter were set to the central value of each range. We adopted a large number of burn-in steps to ensure a negligible dependence on the initial values. To narrow down possible templates, we selected samples with a loose threshold of $\xi < 25$ from all MCMC samples.

Table 4. Template parameters applied in the MCMC method.

Parameter	Range [†]	SD of sampling [‡]
Common		

Table 4 (*continued*)

Parameter	Range [†]	SD of sampling [‡]
Explosion Time t_{exp} (day)	$[-\infty, \infty]$	0.1
Type Ia SN		
Color c	$[-0.2, 0.8]$	0.01
Stretch s	$[0.6, 1.2]$	0.01
Intrinsic Variation I	$[-0.3, 0.3]$	0.01
Type IIL normal		
Peak Magnitude M_B	$[-16.09, -18.05]$	0.01
Color Excess E_{B-V}	$[0, 1]$	0.01
Type IIL bright		
Peak Magnitude M_B	$[-17.92, -19.96]$	0.01
Color Excess E_{B-V}	$[0, 1]$	0.01
Type IIP		
Peak Magnitude M_B	$[-14.43, -18.91]$	0.01
Color Excess E_{B-V}	$[0, 1]$	0.01
Type IIn		
Peak Magnitude M_B	$[-16.98, -20.66]$	0.01
Color Excess E_{B-V}	$[0, 1]$	0.01
Type Ibc normal		
Peak Magnitude M_B	$[-16.09, -18.05]$	0.01
Color Excess E_{B-V}	$[0, 1]$	0.01
Type Ibc bright		
Peak Magnitude M_B	$[-18.46, -20.30]$	0.01
Color Excess E_{B-V}	$[0, 1]$	0.01
Rapid Transient (PS1-10ah)		
Peak Magnitude M_B	$[-16.63, -18.63]$	0.01
Color Excess E_{B-V}	$[0, 1]$	0.01
Rapid Transient (PS1-10bjp)		
Peak Magnitude M_B	$[-17.20, -19.20]$	0.01
Color Excess E_{B-V}	$[0, 1]$	0.01
Rapid Transient (PS1-11bbq)		
Peak Magnitude M_B	$[-18.48, -20.48]$	0.01
Color Excess E_{B-V}	$[0, 1]$	0.01
Rapid Transient (PS1-11qr)		
Peak Magnitude M_B	$[-18.03, -20.03]$	0.01
Color Excess E_{B-V}	$[0, 1]$	0.01
Rapid Transient (PS1-12bb)		
Peak Magnitude M_B	$[-15.29, -17.29]$	0.01
Color Excess E_{B-V}	$[0, 1]$	0.01
Rapid Transient (PS1-12bv)		
Peak Magnitude M_B	$[-18.44, -20.44]$	0.01
Color Excess E_{B-V}	$[0, 1]$	0.01
Rapid Transient (PS1-12brf)		
Peak Magnitude M_B	$[-17.39, -19.39]$	0.01
Color Excess E_{B-V}	$[0, 1]$	0.01
Rapid Transient (PS1-13ess)		
Peak Magnitude M_B	$[-17.49, -19.49]$	0.01
Color Excess E_{B-V}	$[0, 1]$	0.01
Rapid Transient (PS1-13duy)		
Peak Magnitude M_B	$[-17.77, -19.77]$	0.01
Color Excess E_{B-V}	$[0, 1]$	0.01

NOTE—[†] Range of top hat distribution for prior distribution. [‡] Standard deviation of the proposed distribution for sampling.

Table 4 *continued*

Additionally, for the candidates associated with the PS1 extended object (that is, off-center candidates), we confirmed the consistency between the redshifts of transient templates and the distance information of the host galaxies by applying the following criteria:

Criterion 1-1: We eliminated templates whose redshifts were outside the redshift error range (2σ) of the PS1 extended object.

Criterion 1-2: If the PS1 objects exhibited a large angular separation, $\theta_{\text{sep}} > 10''$, we did not apply Criterion 1-1 because the associated PS1 objects were potentially not true host galaxies.

Criterion 2: When $\xi > 25$ for $\theta_{\text{sep}} < 10''$ with Criterion 1-1, we allowed the templates at a redshift larger than that of the PS1 extended objects because a true faint host galaxy may exist behind the PS1 extended object even if $\theta_{\text{sep}} < 10''$.

Here, we used the photometric redshifts (photo- z) from the Sloan Digital Sky Survey (SDSS; York et al. 2000) catalog as the redshift of the PS1 extended object if available. If not, we estimated a single-band redshift z_{single} and its standard deviation σ_z using the following formulae:

$$z_{\text{single}} := \frac{\int_0^\infty \phi A z(D) dD}{\int_0^\infty \phi A dD}, \quad (2)$$

$$\sigma_z^2 := \frac{\int_0^\infty \phi A (z(D) - z_{\text{single}})^2 dD}{\int_0^\infty \phi A dD}, \quad (3)$$

where $\phi = \phi(\lambda, M)$ is the luminosity function of galaxies at a rest wavelength λ derived from the luminosity functions in the $UBVRI$ -band provided in Ilbert et al. (2005) and *Planck* cosmology (Planck Collaboration et al. 2014), $A = A(D)$ is a surface area observed at a distance D , $M = M(D; m_j)$ is an absolute magnitude derived with the j th-band (r or i) apparent magnitude m_j at D in the observer frame, and $\lambda = \lambda(D; \lambda_j)$ is the rest wavelength redshifted from an observed wavelength λ_j at D . We also estimated z_{single} and σ_z for candidates with the SDSS photometric redshift (Table 5). Their comparison illustrates their approximate consistency (Figure 5). Here, we corrected the Galactic extinction (Schlafly & Finkbeiner 2011)³ when we derived absolute magnitudes from apparent magnitudes.

3.2. Results of fitting analysis

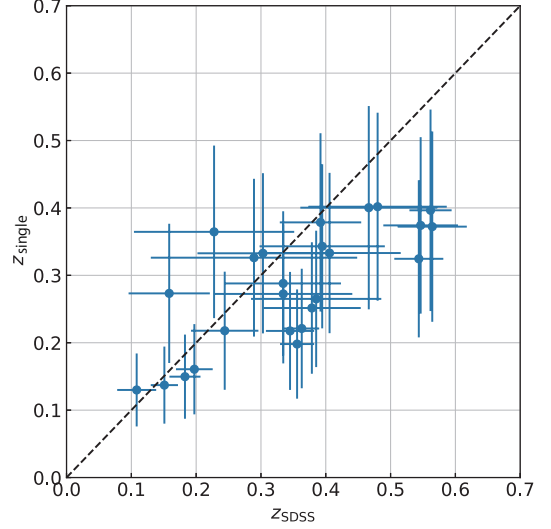


Figure 5. Comparison between the SDSS photometric redshifts and the redshift estimated with Eqs. (2) and (3).

Among the 223 candidates for which we performed light curve fitting, 200 candidates were consistent with the templates of SNe, three candidates were consistent only with the template of RTs, and the remaining 20 candidates were not consistent with any templates or examples. Table 5 shows the coordinates, θ_{sep} , P_{3D} , and probable transient templates of the 200 candidates consistent with the templates. A fitting result of JGEM20ewa with $\xi = 0.6$ is shown as an example of the candidates consistent with the transient template (Figure 6). We concluded that the most probable origin of this candidate is a Type Ia SN for a redshift of $z = 0.25$. The best-fit light curves are shown as solid lines in Figure 6. The top and bottom panels show the PSF flux measured in the stacked and difference images, respectively.

Among the 200 candidates consistent with the templates of SNe, 105 candidates were associated with the PS1 extended objects (that is, off-center candidates), and the remaining 95 candidates had no PS1 extended objects within $< 15''$.

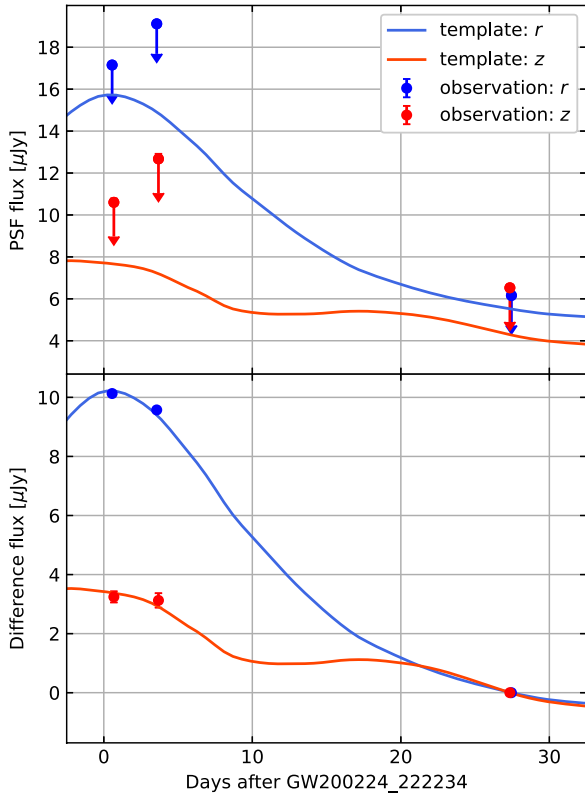
Criterion 1-1 was applied to 102 out of the 105 off-center candidates, and these candidates were excluded from the final candidates. Two of the remaining candidates (JGEM20fvn and JGEM20gqu) were associated with the PS1 extended objects of $z = 0.56 \pm 0.05$ and 0.34 ± 0.04 , respectively. The positions of the candidates and PS1 objects are shown in Figure 7; left (JGEM20fvn) and middle (JGEM20gqu). Because JGEM20fvn and JGEM20gqu exhibited $\theta_{\text{sep}} = 13''.8$

³ <http://irsa.ipac.caltech.edu/applications/DUST/>

Table 5. Information of the candidates that are consistent with the transient templates or examples.

Name	Coordinate (J2000.0)		$\theta_{\text{sep}}^{\dagger}$	z_{single}	σ_z	z_{SDSS}	σ_{SDSS}	$P_{3\text{D}}^{\dagger}$	Probable transient template sets
	R.A. (HH:MM:SS.ss)	Decl. (DD:MM:SS.s)	($''$)						
JGEM20abe	11:43:12.36	−15:39:25.6	8.4	0.37	0.13	—	—	77	CCSNe (Ibc and IIL)
JGEM20abf	11:43:11.52	−15:28:16.3	—	—	—	—	—	—	CCSNe (Ibc, IIn and IIL)
JGEM20acf	11:41:48.24	−14:55:29.3	—	—	—	—	—	—	CCSNe (Ibc, IIn and IIL)
JGEM20adp	11:50:40.82	−15:14:02.8	—	—	—	—	—	—	Type Ia, CCSNe (Ibc, IIn and IIL)
JGEM20adq	11:50:42.55	−15:13:57.4	—	—	—	—	—	—	CCSNe (Ibc, IIn and IIL)
JGEM20ads	11:50:52.06	−15:10:58.4	2.4	0.15	0.06	—	—	97	Type Ia, CCSNe (Ibc, IIn, IIP and IIL)
JGEM20aej	11:49:46.03	−15:01:31.8	—	—	—	—	—	—	Type Ia, CCSNe (Ibc, IIn, IIP and IIL), RTs (13duy)
JGEM20afe	11:48:22.75	−15:44:46.3	12.9	0.33	0.12	—	—	93	CCSNe (Ibc and IIL)
JGEM20cvb	11:40:58.56	−11:26:57.5	2.0	—	—	—	—	—	Type Ia
JGEM20ewa	11:37:13.22	−8:21:04.7	3.6	0.15	0.06	—	—	82	Type Ia
⋮	⋮	⋮	⋮	⋮	⋮	⋮	⋮	⋮	⋮

NOTE—This table is published in its entirety in the machine-readable format. A portion is shown here for guidance regarding its form and content. [†] We indicate “—” if a candidate is not associated with PS1 extended objects.

**Figure 6.** Example of the fitting results. The light curve of JGEM20ewa (points with error bars), and the best-fit light curve of the Type Ia SN template (solid curves); $z = 0.25$, $t_{\text{exp}} = 0.38$ d, $c = -0.15$, $s = 0.60$, and $I = -0.02$. The vertical axes of the top and bottom panels indicate the upper limits measured in the stacked images and the difference fluxes measured in the difference images, respectively.

and $11''.0$ respectively, Criterion 1-2 was applied to

them. We found that the templates of Type Ibc CCSNe with $z = 0.2$ and 0.15 reproduced the light curves of JGEM20fyn and JGEM20gqu, respectively. These results indicated that the PS1 objects associated with JGEM20fyn and JGEM20gqu were unlikely to be true host galaxies and were likely to be Type Ibc CCSNe with $z = 0.2$ and 0.15 . Thus, we ruled out these two objects from the final candidates. Criterion 2 was applied to the remaining one candidate (JGEM20hgo). With Criterion 2, we found that a template of Type Ibc CCSN with $z = 0.1$ can reproduce the light curve of JGEM20hgo. The redshift of the template was larger than the redshift of the PS1 object associated with JGEM20hgo ($z = 0.03 \pm 0.01$). Therefore, we also ruled out JGEM20hgo from the final candidates because it could be a Type Ibc CCSN behind the PS1 object. The stacked and difference images of JGEM20hgo and the associated PS1 object are shown in right panels of Figure 7. The parameters θ_{sep} and $P_{3\text{D}}$ of candidates consistent with the transient templates are shown in Table 5.

Among the 20 candidates inconsistent with the templates, one candidate (JGEM20cvb) exhibited a large ξ value of 2175. However, it apparently matched the template light curve, as shown in Figure 8. This large ξ could be attributed to the underestimation of photometric errors or the uncertainties on the template fluxes. For instance, ξ was improved to ~ 2.4 by assuming a template difference flux error of 0.1 mag. Thus, we concluded that the origin of JGEM20cvb is a Type Ia SN and excluded it from the final candidates.

We also performed template fitting without the single-band photometric redshifts for the candidates associated with extended objects without SDSS photometric redshifts. We found that the redshifts of the best-fit

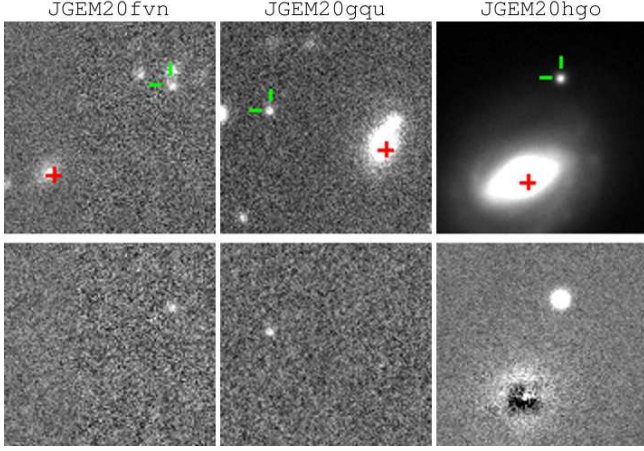


Figure 7. Observed (top) and difference (bottom) r_2 -band images of JGEM20fvn, JGEM20gqu, and JGEM20hgo on February 25, 2020. Each image displays the $20'' \times 20''$ region. Although the PS1 extended objects (plus-shaped markers) are associated with the candidates (reverse L-shaped markers), these are unlikely to be the true host galaxies of the candidates.

templates were consistent for most of the candidates and confirmed that the consistent templates did not change for candidates other than the candidates discussed above, that is, JGEM20fvn, JGEM20gqu, and JGEM20hgo.

As a result, 22 objects, that is, three objects consistent only with RTs and 19 objects inconsistent with all templates and examples, remained as the final candidates of the optical counterpart of GW200224_222234. Their coordinates, θ_{sep} , P_{3D} , and fitting results are shown in Table 6 and Figure 9.

4. SPECTROSCOPIC OBSERVATIONS WITH THE GTC/OSIRIS

Optical spectroscopic observations were performed using the OSIRIS instrument mounted on the 10.4-m GTC telescope located at the Roque de los Muchachos Observatory (Canary Islands, Spain). Five targets were selected for spectroscopic follow-ups to determine the spectroscopic redshift (spec- z) of the probable host galaxies of the candidates. The selected targets were the PS1 extended objects associated with JGEM20fud, JGEM20fyv, JGEM20gdm, JGEM20hdq, and JGEM20hen, which were sufficiently bright in the z -band for short exposures. Owing to observation time constraints, we targeted only these five objects.

The observations were performed on February 10, 2021. The instrumental setup was the spectroscopic

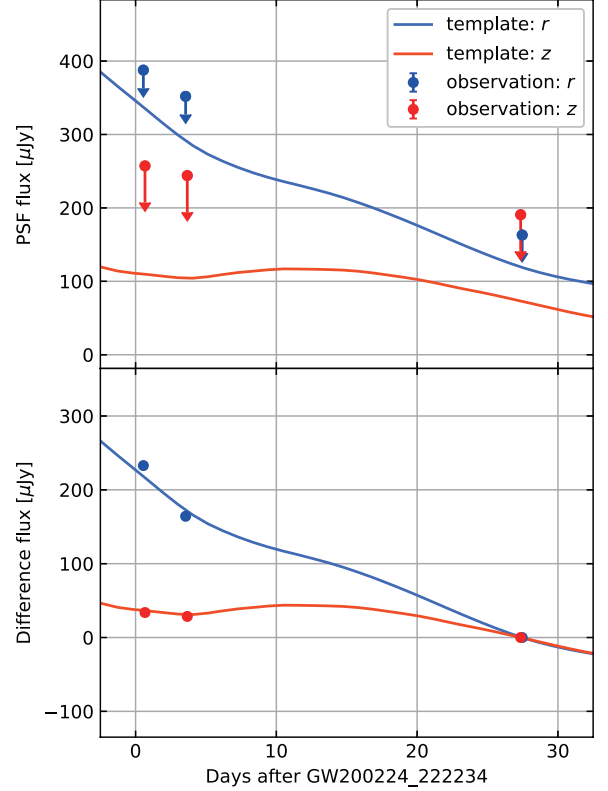


Figure 8. Light curve of JGEM20cvb (points with error bars), and the best-fit light curve of the Type Ia SN template (solid curves); $z = 0.05$, $t_{\text{exp}} = 11.99$ d, color = -0.20 , $s = 1.07$, and $I = 0.05$.

long-slit mode, with a R1000R grism and slit width of 1 arcsec. Each target observation was divided into three exposures of 400 s (1200 s in total for JGEM20fud, JGEM20fyv, and JGEM20hen) and 600 s (1800 s in total for JGEM20gdm and JGEM20hdq). In addition to the targets, the spectrophotometric standard star G191-B2B was also observed using the same instrumental setup and observation conditions. Standard calibration images for bias, flat field, and the calibration lamp (HgAr+Xe+Ne) were also taken during the same night. The data were reduced using standard procedures for bias subtraction, flat-field correction, flux calibration, and atmospheric extinction correction.

The flux calibrated spectra are shown in Figures 10 and 11. The spec- z was derived based on the identification of spectral lines. In addition to the redshifted spectral features from the galaxies, we identified a possible intervening system in the line of sight of JGEM20fud and JGEM20hen, which is consistent with an Mg absorption line located at $z = 0.33$. We show the coordinate, the z -band magnitude, estimated redshift, and spec- z of the target galaxies in Table 7. If an SDSS pho-

Table 6. Information on candidates inconsistent with the templates of SNe and their associated PS1 extended objects.

Name	Coordinate (J2000.0)		$\theta_{\text{sep}}^{\dagger}$	$P_{3\text{D}}^{\dagger}$	Best fitted transient templates
	R.A. (HH:MM:SS.ss)	Decl. (DD:MM:SS.s)	($''$)		
JGEM20acc	11:41:52.70	−15:08:22.9	—	—	CCSN Type Ibc ($\xi \sim 33$)
JGEM20aeh	11:50:20.04	−15:12:54.0	—	—	CCSN Type Ibc ($\xi \sim 55$)
JGEM20boq	11:39:19.68	−12:44:10.0	8.9	75	CCSN Type Ibc ($\xi \sim 334$)
JGEM20bsr	11:37:26.83	−12:05:34.4	—	—	RT 10bjp ($\xi \sim 16$)
JGEM20cpd	11:35:05.23	−11:06:33.8	14.9	94	CCSN Type Ibc ($\xi \sim 281$)
JGEM20dig	11:41:48.72	−11:45:02.9	11.4	78	CCSN Type Ibc ($\xi \sim 26$)
JGEM20dte	11:27:56.54	−9:05:45.6	—	—	CCSN Type Ibc ($\xi \sim 159$)
JGEM20ejv	11:47:24.98	−9:40:32.5	6.3	75	CCSN Type Ibc ($\xi \sim 62$)
JGEM20ekz	11:45:32.81	−9:42:04.7	—	—	CCSN Type Ibc ($\xi \sim 84$)
JGEM20env	11:33:13.03	−8:10:35.0	14.3	—	CCSN Type IIL ($\xi \sim 331$)
JGEM20enw	11:32:50.98	−7:56:35.2	14.9	74	RT 13duy ($\xi \sim 1$)
JGEM20eso	11:28:42.14	−7:48:41.4	—	—	RT 13duy ($\xi \sim 10$)
JGEM20fci	11:44:18.89	−8:08:34.4	—	—	Type Ia SN ($\xi \sim 1137$)
JGEM20fud	11:31:23.86	−5:55:16.0	7.0	89	Type Ia SN ($\xi \sim 1562$)
JGEM20fxo	11:40:19.39	−6:36:34.9	—	—	CCSN Type Ibc ($\xi \sim 77$)
JGEM20fyv	11:40:00.36	−6:01:27.5	5.2	99	CCSN Type Ibc ($\xi \sim 422$)
JGEM20gdm	11:45:52.56	−6:13:49.4	1.6	91	CCSN Type IIL ($\xi \sim 27$)
JGEM20hdq	11:32:35.04	−3:56:15.7	3.0	60	RT 10bjp ($\xi \sim 187$)
JGEM20hea	11:32:20.45	−3:40:50.9	3.7	60	CCSN Type Ibc ($\xi \sim 394$)
JGEM20hen	11:32:21.91	−3:09:21.6	7.3	98	Type Ia SN ($\xi \sim 348$)
JGEM20hfc	11:31:30.55	−3:45:54.7	2.7	94	CCSN Type Ibc ($\xi \sim 87$)
JGEM20hkw	11:35:25.49	−4:11:36.6	—	—	CCSN Type Ibc ($\xi \sim 37$)

NOTE—[†] We indicate “—” if a candidate is not associated with PS1 extended objects.

tometric redshift is not available, we show z_{single} and σ_z calculated with Equations (2) and (3). However, note that these have large uncertainties because they are calculated from only a single band magnitude.

Figure 12 shows the 2D location and distance of the five candidates. We evaluated their associations with GW200224.222234 by comparing the 3D location of their probable host galaxies with the 3D skymap of GW200224.222234. Here, we define the probability of the association as follows:

$$P_{\text{assoc}}(x_{\text{gal}}) := 1 - \int_{f_x > f_{x_{\text{gal}}}} f_x dV_x, \quad (4)$$

where f_x is the probability distribution function (PDF) at the 3D coordinates x , and x_{gal} is the location of the host galaxy. The integration in Equation (4) represents the cumulative probability integrated over the region with $f_x > f_{x_{\text{gal}}}$. The PDF was obtained as $f_x = \rho(\text{R.A.}, \text{Decl.}) N(D; \mu, \sigma^2)$ using the 2D probability distribution $\rho = \rho(\text{R.A.}, \text{Decl.})$ and normal distribution $N(D; \mu, \sigma^2)$ of the distance with the mean $\mu = \mu(\text{R.A.}, \text{Decl.})$ and standard deviation $\sigma = \sigma(\text{R.A.}, \text{Decl.})$ provided for each direction. To perform the integration of Equation (4) numerically, we discretized $N(D)$ into 5000 bins from 0 to 50000 Mpc. The

discretization of ρ was performed through pixelization using HEALPix. P_{assoc} is small when the host galaxy is located outside the highly probable region. We set the threshold to $P_{\text{assoc}} = 0.01$. Table 7 also shows P_{assoc} obtained for the five targets. Although JGEM20gdm, JGEM20hdq, and JGEM20hen were located outside the highly probable region ($P_{\text{assoc}} < 0.01$) and are unlikely to be related to GW200224.222234, JGEM20fud and JGEM20fyv were close to the highly probable region ($P_{\text{assoc}} = 0.76$ and 0.07 , respectively) and thus are possible counterparts of GW200224.222234.

5. DISCUSSION

5.1. Contamination from supernovae

Next, we evaluated our detection criteria and screening process by comparing our results with the expected number of SN detections. We estimated the expected number of SN detections by summing up mock-SN samples weighted with cosmological histories of SN rates using the observation depth, as in Niino et al. (2014) and Ohgami et al. (2021). We assumed the SN rate of Okumura et al. (2014) and Dahlen et al. (2012) for the Type Ia SN and CCSN, respectively. For the Type

Table 7. Information of the target galaxies.

Name	Coordinate of the target galaxy (J2000.0)		m_z^\dagger	Estimated	spec- z	P_{assoc}
	R.A. (HH:MM:SS.ss)	Decl. (DD:MM:SS.s)	(mag)	Redshift		
JGEM20fud	11:31:24.32	−05:55:17.8	18.7	$0.22 \pm 0.03^\ddagger$	0.357	0.76
JGEM20fyv	11:40:00.36	−06:01:22.1	19.0	$0.26 \pm 0.07^*$	0.391	0.07
JGEM20gdm	11:45:52.63	−06:13:48.4	19.9	$0.29 \pm 0.09^*$	0.398	1×10^{-3}
JGEM20hdq	11:32:35.03	−03:56:18.6	20.1	$0.56 \pm 0.03^\ddagger$	0.632	1×10^{-8}
JGEM20hen	11:32:22.41	−03:09:22.9	18.4	$0.36 \pm 0.03^\ddagger$	0.438	4×10^{-3}

NOTE—[†] z -band magnitude of the target galaxy from the PS1 catalog. [‡] Photometric redshift z_{SDSS} from the SDSS catalog. [*] z_{single} and σ_z calculated with Eqs. (2) and (3).

Ia SN, the SN light curves were generated from the evolution of the SN spectrum provided by Hsiao et al. (2007). For the CCSN, the light curves were generated from the templates provided by Nugent et al. (2002)⁴. We referred to the luminosity distributions of SNe in Barbary et al. (2012) and Dahlen et al. (2012).

Because our observation depth in the z -band was shallower than that in the r -band, most of candidates were detected only in the r -band. Thus, we sampled mock SNe whose brightness was decaying in the r -band, assuming the reference images were taken 27 d after detection because the variation in the SN magnitude during 3 d between Days 1 and 4 (< 0.1 mag) was negligible compared to the standard deviation of the 5σ limiting magnitude of our observation. The number density as a function of limiting magnitude is shown in Figure 13 as a dashed curve. The colored area represents the $\pm 50\%$ error from the 1σ error of the CCSN rate density. In the actual observation, the detection completeness for fainter sources was lower (Figure 3). Therefore, we considered two detections based on the completeness of Day 1–28 and Day 4–28. The solid curve in Figure 13 is the number density derived by considering the completeness. The dot with error bars was estimated with the number of transients consistent with SNe, $N_{\text{SN}} = 201$, and our observed area of $S = 56.6 \text{ deg}^2$. The vertical error bar was defined as $\sqrt{N_{\text{SN}}}/S$ by assuming that the number followed a Poisson distribution with the expected value of N_{SN} . The horizontal error bar is the 1σ error of the 5σ limiting magnitude in the difference images on Day 4 in the $r2$ -band.

Our result is consistent with the expected number density of SN detection within a 1σ error. This verified that our detection criteria and screening process can be used to identify SNe with high completeness. Note that our

result was located at the 1σ lower end of the expected value. This might be because we ignored nuclear transients in this search.

5.2. Implication in BBH merger models accompanied by EM emissions

We finally found 19 candidates of the optical counterpart of GW200224_222234 by performing light curve fitting and spectroscopic observations. Owing to the limitation of observations, we must exclude sources located at the center of galaxies, and thus these final candidates cannot be considered variabilities of galactic nuclei, such as a kicked BBH merger in an accretion disk shown by McKernan et al. (2019). Yamazaki et al. (2016) reported a BBH merger potentially accompanied by γ -ray emissions caused by a relativistic outflow. They showed that optical afterglow peaks appear $\sim 4.5 \times 10^4$ s after GW detection (almost the same as the start of our first epoch observation) if the ambient matter density is 0.01 cm^{-3} ; however, the peak flux is expected to be lower than our observation limits ($0.37 \mu\text{Jy}$ in r -band) at a distance of 1710 Mpc. Therefore, such afterglow could not be detected in our search.

Among the 19 candidates, 16 candidates inconsistent with all templates and examples exhibited the increasing difference flux in one band and the decreasing difference flux in another band (for example, JGEM20ejv), or a more rapid decline in the z -band than in the r -band (for example, JGEM20boq). If we perform further observations to obtain deeper images than the current reference images after the candidates sufficiently decay, we can measure the genuine fluxes of these candidates instead of the difference fluxes and hence identify their natures.

The final 19 candidates are potentially unrelated to GW200224_222234. If there are no counterparts of GW200224_222234, the upper limits of optical luminosity are $\nu L_\nu < 5.2_{-1.9}^{+2.4} \times 10^{41} \text{ erg s}^{-1}$ ($9.1_{-3.3}^{+4.1} \times 10^{41} \text{ erg s}^{-1}$) and $\nu L_\nu < 1.8_{-0.6}^{+0.8} \times 10^{42} \text{ erg s}^{-1}$ ($2.4_{-0.9}^{+1.1} \times 10^{42} \text{ erg s}^{-1}$).

⁴ The light curve templates of Type Ia SNe and CCSNe are available at the website https://c3.lbl.gov/nugent/nugent_templates.html.

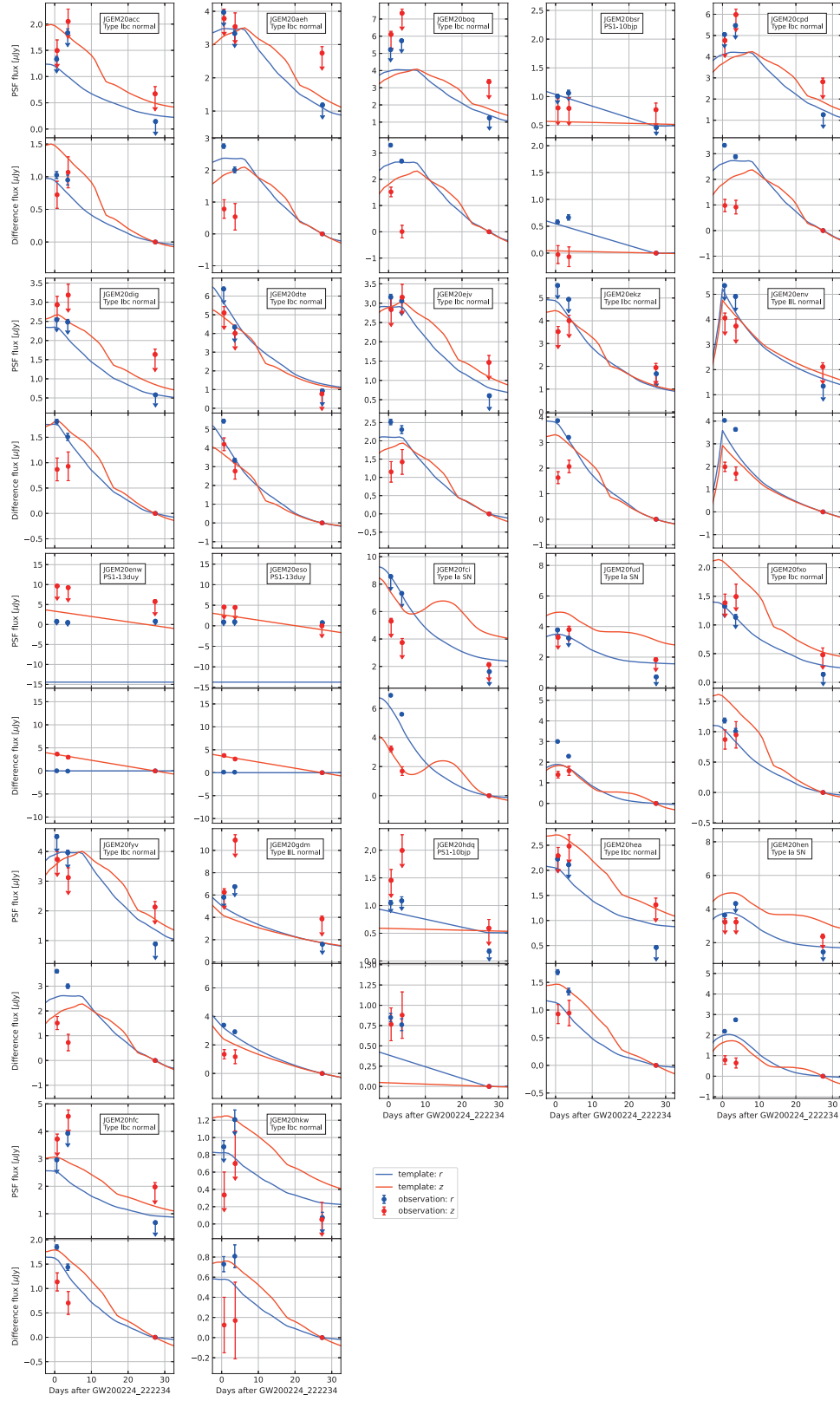


Figure 9. Light curves of 19 candidates inconsistent with the templates of SNe and three candidates consistent only with RTs. The best-fit (but bad-fit for the former 19 candidates) templates or examples are also shown for comparison. The vertical axis of each panel indicates the upper limits measured in the stacked images (top) and the difference fluxes measured in the difference images (bottom).

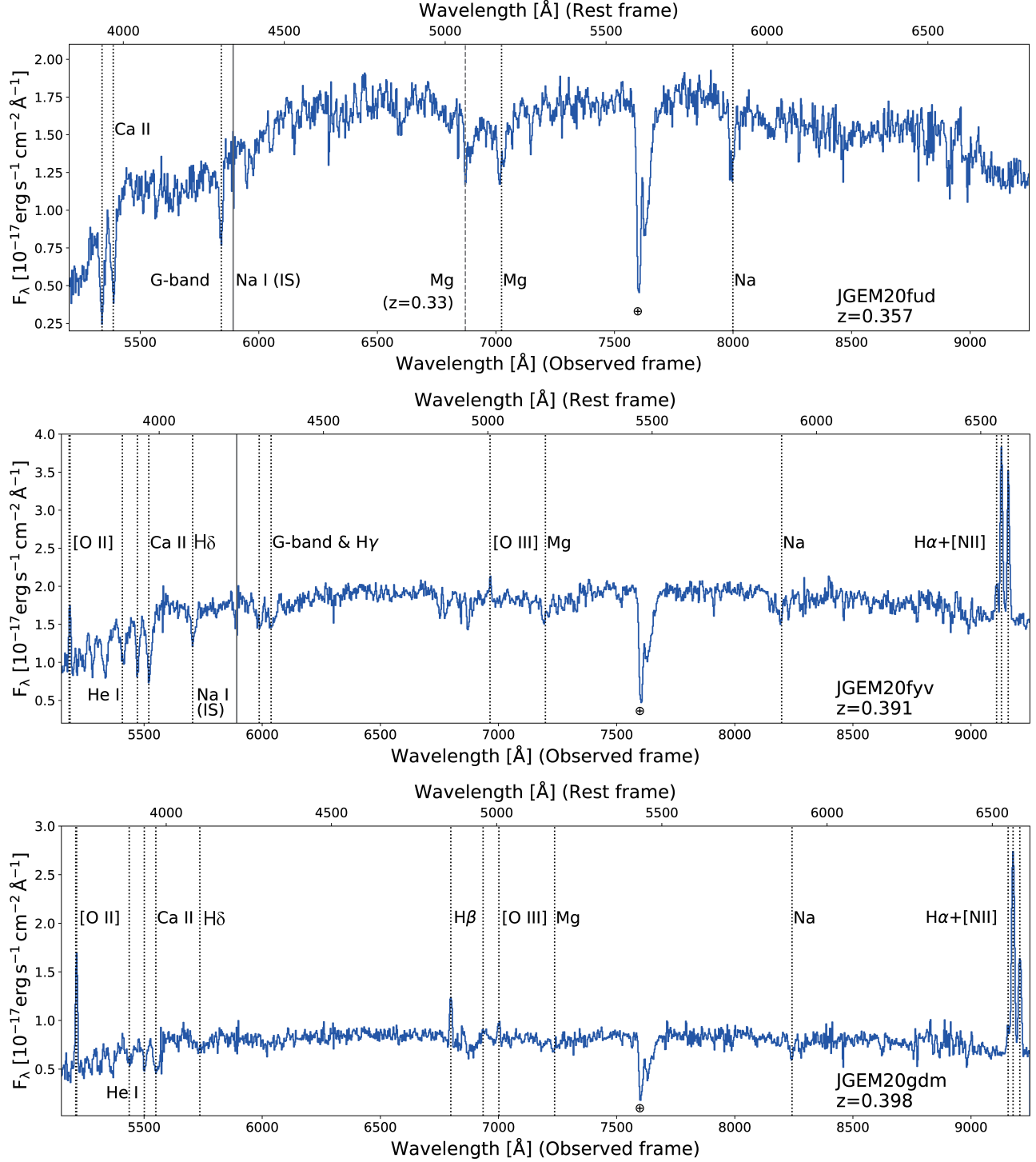


Figure 10. Optical spectra of candidates JGEM20fud, JGEM20fyv, JGEM20gdm, JGEM20hdq, and JGEM20hen observed with GTC. The identified spectral features are marked by vertical dotted lines. The Na interstellar absorption feature is denoted by a solid vertical line. The emission lines identified as intervening systems are marked by dashed lines.

erg s^{-1}) on Day 1 (Day 4) in the r 2-band and z -band, respectively. Note that these upper limits are comparable with the luminosity of a possible EM counterpart of the

BBH event GW190521 ($10^{42} \text{ erg s}^{-1}$, McKernan et al. 2019).

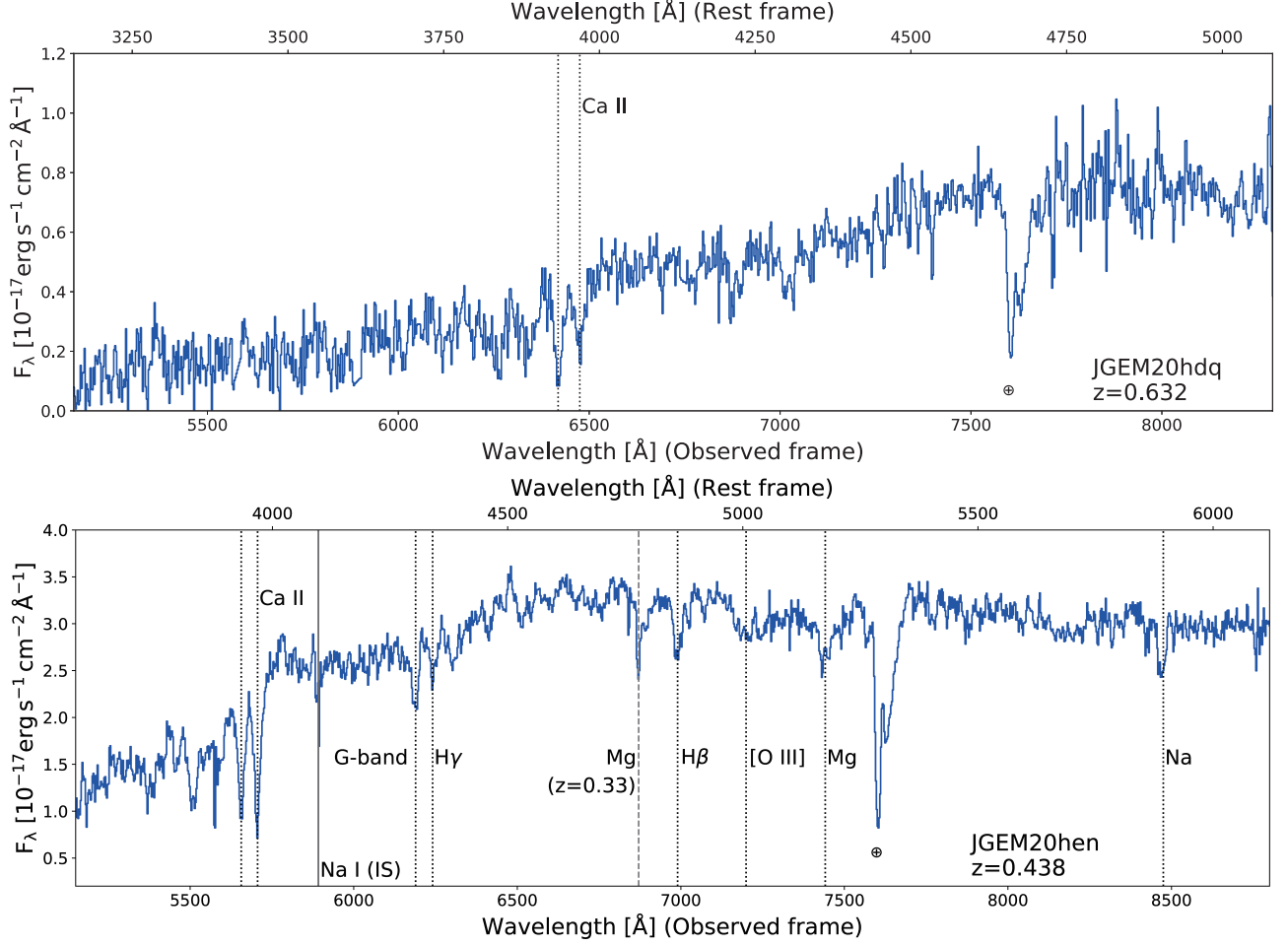


Figure 11. Continuation of Figure 10.

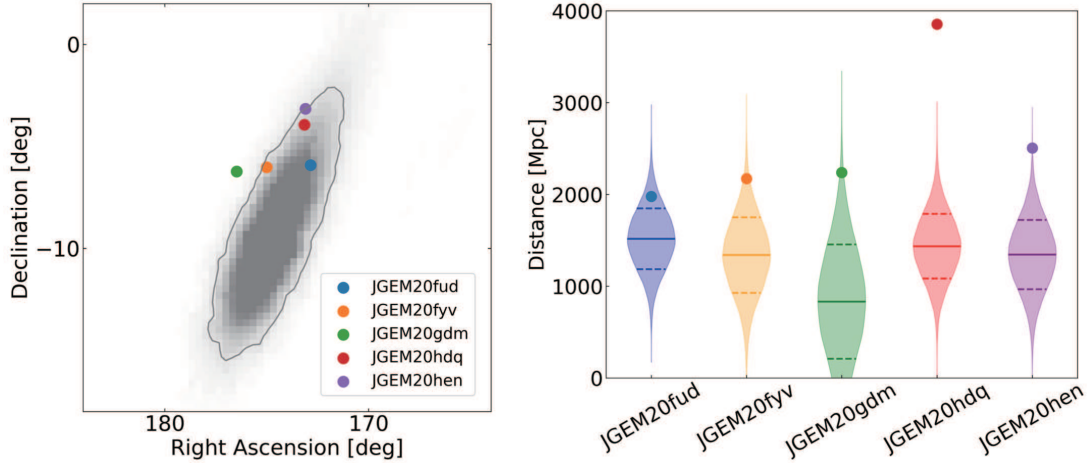


Figure 12. (Left) 2D location of the five candidates observed with the GTC/OSIRIS and the localization skymap (IMRPhenomXPHM model) released in the GWTC-3 catalog. The dots are the locations of the candidates. The gray contour line indicates the 90% credible region. (Right) Distance of each candidate and probability distribution at their location as a function of distance. The dots are the distances of the candidates. The horizontal solid and dashed lines indicate the mean and standard deviation of the probability distribution, respectively.

5.3. Comparison with sources detected by other observations

For GW200224_222234, the Neil Gehrels Swift Observatory performed near-UV/X-ray observations cov-

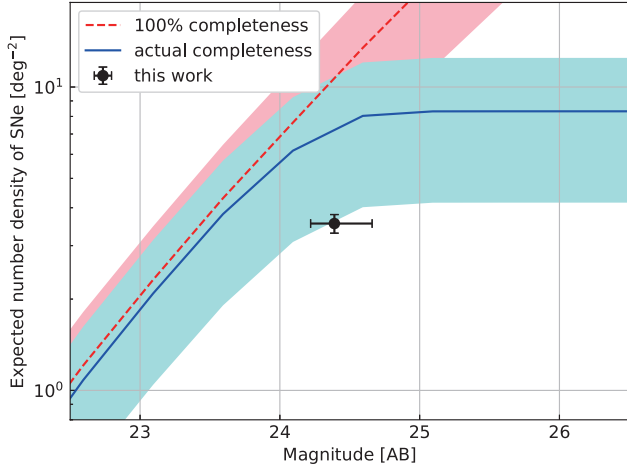


Figure 13. Expected number density of SN detection in the r -band as a function of limiting magnitude. The colored area is the $\pm 50\%$ error originating from the 1σ error of the core-collapse-SN rate density. The dashed curve was obtained with 100% completeness, and the solid curve was obtained with the actual completeness of our survey, shown in Figure 3, under the assumption of twice detection. The dot with error bars was obtained using the number density of the transients consistent with the templates of SNe. The vertical error bar is defined as $\sqrt{N_{\text{SN}}}/S$ by assuming that the number follows a Poisson distribution with the expected value of N_{SN} . The horizontal error bar is the 1σ error of the 5σ limiting magnitude in the difference images on Day 4 in the r_2 -band.

ering an area corresponding to 79.2%/62.4% of the GW probability region and reported their detection of eight X-ray sources and three near-UV sources (Klingler et al. 2021; Oates et al. 2021), whereas no significant signal was detected in very high-energy γ -ray (Abdalla et al. 2021). We searched our sources to find out whether these sources were detected. The source JGEM20aoz was located at R.A. = $11^{\text{h}}41^{\text{m}}41^{\text{s}}.81$, Decl. = $-14^{\circ}07'54''.78$ (J2000.0), 4.8 arcsec off center of the error circle of X-ray Source 7. JGEM20aoz was detected four times (two epochs and two bands) and exhibited a magnitude of 21.75 mag (21.59 mag) and 21.43 mag (21.25 mag) in the r - and z -bands, respectively, in the first (second) epoch difference images. However, we classified it as a star-like object and ruled it out because the coordinates matched that of a point source found in the PS1 catalog. In the SIMBAD archival database, a BL Lac-type object (2FGL J1141.7-1404) is located at a position consistent with JGEM20aoz. Therefore, we conclude that JGEM20aoz is likely an AGN.

Our observation area also covered part of the area observed by the GW program in the Dark Energy

Survey (DESGW). They conducted observations of GW200224_222234 using the Dark Energy Camera (DECam) in the i -band on February 24, 25, 27, and March 5, 2020, with 10σ limiting magnitudes of 23.17, 23.19, 23.49, and 23.03, respectively, and reported eight transients (Morgan et al. 2020). Comparing the transients found by the DESGW with our candidates, JGEM20gfn matched the coordinates of AT2020ehw within $1''$. JGEM20gfn was classified as an SN via light curve fitting. We could not detect AT2020eho and AT2020eht because they were located at the CCD gap of our difference images. Sources were detected at the location of AT2020ehp and AT2020ehq in our difference images, but they were rejected because of the large elongation, $(b/a)/(b/a)_{\text{PSF}} = 0.6$ and 0.5 , respectively. Although no source was found at the position of AT2020ehy in both the stacked and difference images, AT2020ehv and AT2020ehr were observed in the stacked images but could not be detected in the difference images with our criterion $(S/N)_{\text{PSF}} > 5$.

5.4. Comparison with a kilonova light curve

Although GW200224_222234 was classified as a BBH merger, we compared our observation result with a kilonova model based on a radiative transfer simulation with an ejecta mass $M_{\text{ej}} = 0.05 M_{\odot}$ and an electron fraction $Y_e = 0.30 - 0.40$ (Banerjee et al. 2020). This kilonova model can explain the observed early multi-color light curve of GW170817/AT2017gfo. The peak of bolometric luminosity approximately scales with M_{ej} to the power of 0.35 (see Fernández & Metzger 2016; Metzger 2019; Tanaka 2016). Y_e influences the light curves through the opacity. In the low- Y_e case ($Y_e < 0.25$), the kilonova ejecta becomes Lanthanide rich and the opacity becomes higher, and thus the light curves in the early phase can be fainter by 2 – 3 mag than that in the adopted model of $Y_e = 0.30 - 0.40$.

Figure 14 shows a comparison between the kilonova light curve and the magnitudes of two candidates whose host galaxies’ spectroscopic redshifts are consistent with the 3D skymap of GW200224_222234 (JGEM20fud and JGEM20fyv). All observed magnitudes were brighter and more slowly decaying than the kilonova at the distance of the host galaxies. They did not exhibit rapid decline in short-wavelength components, being a major feature of the kilonova model; thus, they are unlikely to be kilonovae.

5.5. Future prospects

Here, we discuss the future prospects of follow-ups for kilonova events with the Subaru/HSC in the era of next-generation GW interferometers, such as an optimal

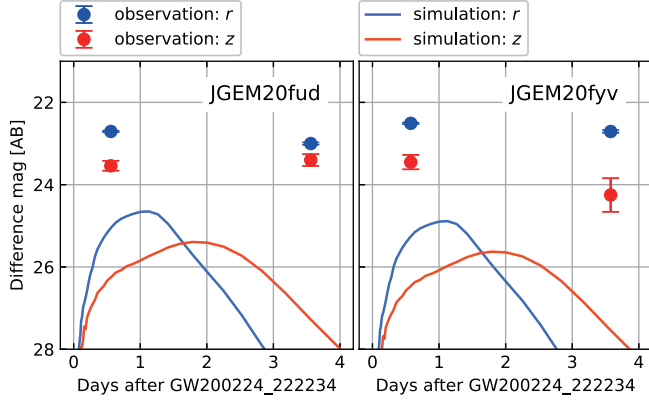


Figure 14. Comparison of light curves between the candidates whose host galaxies’ spectroscopic redshifts are consistent with the 3D skymap of GW200224_222234 and a kilonova model with an ejecta mass $M_{\text{ej}} = 0.05 M_{\odot}$ and an electron fraction $Y_e = 0.30 - 0.40$ (Banerjee et al. 2020). We assume the kilonovae are located at the distance of each candidate.

upgrade of the LIGO facilities, known as “Voyager.” If a BNS merger occurs at the distance of GW200224_222234 (~ 1710 Mpc), can we detect it?

Figure 15 shows the r -, i -, and z -band light curves under an assumption that the kilonova is located at the estimated distance of GW200224_222234. The colored area is the uncertainty caused by the 1σ credible range of the distance. The horizontal lines with the upward arrows are the 5σ limiting magnitudes measured in the difference images in each epoch in each band (r and z). In the r -band, although the observation depth in the first epoch was sufficiently deep to detect the rising phase of the light curve, the model light curve decreased rapidly and was significantly fainter than the limiting magnitude in the second epoch. The observation depths in the z -band did not reach the brightness in either epoch. Thus, if a BNS merger occurs at the distance of GW200224_222234, we might be able to detect the light curve in the early phase in the r -band using the power of a wide-field survey with an 8-m telescope.

Based on the follow-up of GW200224_222234, the number of sources detected only on Day 1 and only in the $r2$ -band (excluded using detection criterion (v)) reached 20137⁵. It is difficult to determine their origin using only single epoch and single band data.

Next, we consider what will improve the detection efficiency of future surveys. (1) If we adopt a high-cadence (one day) and continuous (over three days) observation,

⁵ This number includes bogus detections because we did not perform visual inspection.

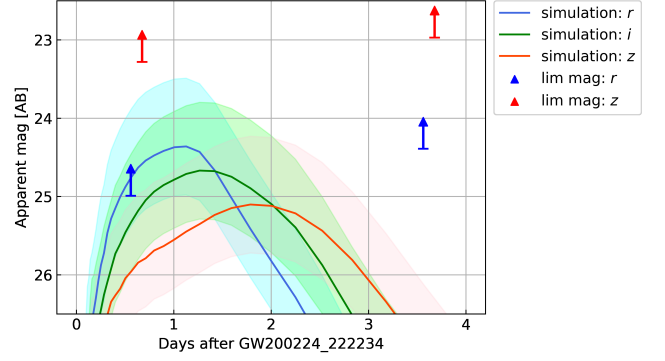


Figure 15. Comparison between a kilonova model located at the estimated distance of the GW200224_222234 and the limiting magnitudes of our observation. The solid curves are the light curves of the kilonova model, the same as in Figure 14. The colored area represents the uncertainty caused by the 1σ credible range of the distance.

the kilonova at this distance will be detected on Days 1 and 2 and not detected on Day 3 in the r -band. This will illustrate the rapidly evolving nature of the kilonova. (2) If we adopt the i -band instead of the z -band, the i -band observation with Subaru/HSC will reach ~ 24 mag with 1 min of exposure and may detect the kilonova on Day 2. This will constrain the color of the kilonova. These considerations illustrate the power of a dedicated wide-field search with an 8m-class telescope, such as Subaru/HSC and Rubin/Legacy Survey of Space and Time (LSST).

6. SUMMARY & CONCLUSION

The BBH coalescence GW200224_222234 was detected by the LIGO/Virgo collaboration with their three detectors on February 24, 2020. We performed ToO observations using the Subaru/HSC in the $r2$ - and z -bands during three epochs: February 24, 28, and March 23, 2020. We selected the observation area from the high-probability region in the preliminary localization skymap covering 56.6 deg^2 . The integrated probability reaches 91% in the localization skymap released in the GWTC-3 catalog.

We searched for the optical counterpart using the image subtraction technique. We adopted the images taken on the third epoch as the reference images and obtained the difference images of the first and second epochs. After screening for the sources detected in the difference images via matching with the PS1 catalog and visual inspection, we found 223 candidates. We could not include sources located at the galactic center owing to the limitations of observation. Subsequently, we classified these candidates using their angular separation from the nearby extended object and distance estimated from the photometric data. Additionally, we investigated their

nature using light curve fitting with the transient template set. We adopted the templates of the Type Ia SN and CCSN and examples of RTs and then found 201 candidates consistent with the SN templates and likely not related to GW200224_222234.

To measure the spectroscopic redshifts of the probable host galaxies of the final candidates, we also performed spectroscopic observations using the GTC/OSIRIS for the extended PS1 objects associated with the five candidates. We found that two targets (JGEM20fud and JGEM20fyv) are likely to be located inside the highly probable region. The other targets are outside the highly probable region and not related to the GW event.

As a result, we found 19 candidates as possible candidates of the optical counterpart of GW200224_222234. The light curves of three candidates were consistent only with those of RTs, and the light curves of the other 16 candidates were inconsistent with all transients and examples. These 19 candidates have a potential for being unrelated to GW200224_222234; however, we could not establish their nature because of the lack of spectroscopic observations for the candidates. If there is no counterpart of GW200224_222234 in the 19 final candidates, the upper limits of optical luminosity are evaluated as $\nu L_\nu < 5.2_{-1.9}^{+2.4} \times 10^{41} \text{ erg s}^{-1}$ ($9.1_{-3.3}^{+4.1} \times 10^{41} \text{ erg s}^{-1}$) and $\nu L_\nu < 1.8_{-0.6}^{+0.8} \times 10^{42} \text{ erg s}^{-1}$ ($2.4_{-0.9}^{+1.1} \times 10^{42} \text{ erg s}^{-1}$) on Day 1 (Day 4) in the r 2-band and z -band, respectively, from the 5σ limiting magnitudes of our observation. These upper limits are comparable with the brightness of a possible EM counterpart of the BBH event GW190521 ($10^{42} \text{ erg s}^{-1}$, McKernan et al. 2019).

We evaluated our detection criteria and screening process by comparing our result with the expected number of SN detections, which was estimated from a cosmic SN rate. The number density of the candidates consistent with the SN templates was consistent with the expected number density within a 1σ error. This indicated that our method could identify SNe with high completeness.

We also compared our sources with those found by the *Swift* and DESGW and found that some of our sources were associated with their sources. However, these identical sources are unlikely to be the optical counterpart of the GW.

Additionally, we discuss the implications of our result in several models of a BBH merger accompanied by EM emissions. The kicked BBH merger in an accretion disk reported by McKernan et al. (2019) cannot be a possible nature of the 16 candidates inconsistent with all transients because we excluded nucleus transients. The relativistic outflow model reported in Yamazaki et al. (2016) also cannot be a possible nature of the candidates because the expected flux is fainter than the 5σ

limiting magnitude of our observations. It is important to perform further observations deeper than the observations on Day 28 to identify their nature.

We also compared the light curve of the two candidates with the kilonova light curve by adopting a radiative transfer simulation that could explain the multi-color light curve of GW170817/AT2017gfo. These candidates likely did not originate from the same kilonova as AT2017gfo because these were brighter and more slowly decaying than the kilonova. We also discuss future prospects by comparing our observation depths with the kilonova light curve. If we perform a high-cadence (one day) and continuous (over three days) observation, we can reveal the rapidly evolving nature of transients. Moreover, our observation can detect a kilonova or a possible EM counterpart of the BBH event GW190521 (McKernan et al. 2019) at the distance of GW200224_222234. This demonstrates the power of 8m-class telescopes, such as Subaru/HSC and Rubin/LSST.

These collaborative observations were possible thanks to the leadership of the National Astronomical Observatory of Japan (NAOJ) and the Instituto de Astrofísica de Canarias (IAC). This research was based in part on data collected at the Subaru Telescope, which is operated by the NAOJ, and in part on observations made using the GTC telescope in the Spanish Observatorio del Roque de los Muchachos of IAC under Director's Discretionary Time. The spectroscopic data were obtained using the instrument OSIRIS, built by a Consortium led by the Instituto de Astrofísica de Canarias in collaboration with the Instituto de Astronomía of the Universidad Autónoma de México. OSIRIS was funded by GRANTECAN and the National Plan of Astronomy and Astrophysics of the Spanish Government. We are grateful to the staff of the Subaru Telescope for their help with the observations of this study. We are honored and grateful for the opportunity to observe the Universe from Maunakea, which has cultural, historical, and natural significance in Hawaii. This study was supported by MEXT KAKENHI (JP17H06363) and JSPS KAKENHI (JP19H00694, JP20H00158, JP20H00179, JP21H04997). JBG, FP, JAAP, IPF, and TMD acknowledge financial support from the Spanish Ministry of Science and Innovation (MICINN) through the Spanish State Research Agency, under Severo Ochoa Program 2020-2023 (CEX2019-000920-S) and the projects PID2019-107988GB-C22 and PID2019-105552RB-C43. We would like to thank Editage (www.editage.com) for English language editing.

Facilities: Subaru (HSC), GTC(OSIRIS)

Software: hscPipe (Bosch et al. 2018), astropy (Astropy Collaboration et al. 2013, 2018), Source Extractor (Bertin & Arnouts 1996)

REFERENCES

- Abbott, B. P., Abbott, R., Abbott, T. D., et al. 2017, ApJL, 848, L12, doi: [10.3847/2041-8213/aa91c9](https://doi.org/10.3847/2041-8213/aa91c9)
- Abdalla, H., Aharonian, F., Ait Benkhali, F., et al. 2021, ApJ, 923, 109, doi: [10.3847/1538-4357/ac2e04](https://doi.org/10.3847/1538-4357/ac2e04)
- Alard, C. 1999, arXiv e-prints, astro.
<https://arxiv.org/abs/astro-ph/9903111>
- Alard, C., & Lupton, R. H. 1998, ApJ, 503, 325, doi: [10.1086/305984](https://doi.org/10.1086/305984)
- Andreoni, I., Ackley, K., Cooke, J., et al. 2017, Publications of the Astronomical Society of Australia, 34, e069, doi: [10.1017/pasa.2017.65](https://doi.org/10.1017/pasa.2017.65)
- Arcavi, I., McCully, C., Hosseinzadeh, G., et al. 2017, ApJL, 848, L33, doi: [10.3847/2041-8213/aa910f](https://doi.org/10.3847/2041-8213/aa910f)
- Astropy Collaboration, Robitaille, T. P., Tollerud, E. J., et al. 2013, A&A, 558, A33, doi: [10.1051/0004-6361/201322068](https://doi.org/10.1051/0004-6361/201322068)
- Astropy Collaboration, Price-Whelan, A. M., Sipőcz, B. M., et al. 2018, AJ, 156, 123, doi: [10.3847/1538-3881/aabc4f](https://doi.org/10.3847/1538-3881/aabc4f)
- Banerjee, S., Tanaka, M., Kawaguchi, K., Kato, D., & Gaigalas, G. 2020, ApJ, 901, 29, doi: [10.3847/1538-4357/abae61](https://doi.org/10.3847/1538-4357/abae61)
- Barbary, K., Aldering, G., Amanullah, R., et al. 2012, ApJ, 745, 31, doi: [10.1088/0004-637X/745/1/31](https://doi.org/10.1088/0004-637X/745/1/31)
- Bartos, I., Kocsis, B., Haiman, Z., & Márka, S. 2017, ApJ, 835, 165, doi: [10.3847/1538-4357/835/2/165](https://doi.org/10.3847/1538-4357/835/2/165)
- Bertin, E., & Arnouts, S. 1996, A&AS, 117, 393, doi: [10.1051/aas:1996164](https://doi.org/10.1051/aas:1996164)
- Bosch, J., Armstrong, R., Bickerton, S., et al. 2018, PASJ, 70, S5, doi: [10.1093/pasj/psx080](https://doi.org/10.1093/pasj/psx080)
- Chornock, R., Berger, E., Kasen, D., et al. 2017, ApJL, 848, L19, doi: [10.3847/2041-8213/aa905c](https://doi.org/10.3847/2041-8213/aa905c)
- Connaughton, V., Burns, E., Goldstein, A., et al. 2016, ApJL, 826, L6, doi: [10.3847/2041-8205/826/1/L6](https://doi.org/10.3847/2041-8205/826/1/L6)
- Coulter, D. A., Foley, R. J., Kilpatrick, C. D., et al. 2017, Science, 358, 1556, doi: [10.1126/science.aap9811](https://doi.org/10.1126/science.aap9811)
- Cowperthwaite, P. S., Berger, E., Villar, V. A., et al. 2017, ApJL, 848, L17, doi: [10.3847/2041-8213/aa8fc7](https://doi.org/10.3847/2041-8213/aa8fc7)
- Dahlen, T., Strolger, L.-G., Riess, A. G., et al. 2012, ApJ, 757, 70, doi: [10.1088/0004-637X/757/1/70](https://doi.org/10.1088/0004-637X/757/1/70)
- Díaz, M. C., Macri, L. M., Garcia Lambas, D., et al. 2017, ApJL, 848, L29, doi: [10.3847/2041-8213/aa9060](https://doi.org/10.3847/2041-8213/aa9060)
- Drout, M. R., Chornock, R., Soderberg, A. M., et al. 2014, ApJ, 794, 23, doi: [10.1088/0004-637X/794/1/23](https://doi.org/10.1088/0004-637X/794/1/23)
- Drout, M. R., Piro, A. L., Shappee, B. J., et al. 2017, Science, 358, 1570, doi: [10.1126/science.aaq0049](https://doi.org/10.1126/science.aaq0049)
- Einstein, A. 1916, Sitzungsberichte der Königlich Preußischen Akademie der Wissenschaften (Berlin), 688
- . 1918, Sitzungsberichte der Königlich Preußischen Akademie der Wissenschaften (Berlin), 154
- Evans, P. A., Cenko, S. B., Kennea, J. A., et al. 2017, Science, 358, 1565, doi: [10.1126/science.aap9580](https://doi.org/10.1126/science.aap9580)
- Fernández, R., & Metzger, B. D. 2016, Annual Review of Nuclear and Particle Science, 66, 23, doi: [10.1146/annurev-nucl-102115-044819](https://doi.org/10.1146/annurev-nucl-102115-044819)
- Flewelling, H. A., Magnier, E. A., Chambers, K. C., et al. 2020, ApJS, 251, 7, doi: [10.3847/1538-4365/abb82d](https://doi.org/10.3847/1538-4365/abb82d)
- Furusawa, H., Koike, M., Takata, T., et al. 2018, PASJ, 70, S3, doi: [10.1093/pasj/psx079](https://doi.org/10.1093/pasj/psx079)
- Graham, M. J., Ford, K. E. S., McKernan, B., et al. 2020, PhRvL, 124, 251102, doi: [10.1103/PhysRevLett.124.251102](https://doi.org/10.1103/PhysRevLett.124.251102)
- Graham, M. J., McKernan, B., Ford, K. E. S., et al. 2022, arXiv e-prints, arXiv:2209.13004.
<https://arxiv.org/abs/2209.13004>
- Hsiao, E. Y., Conley, A., Howell, D. A., et al. 2007, ApJ, 663, 1187, doi: [10.1086/518232](https://doi.org/10.1086/518232)
- Ilbert, O., Tresse, L., Zucca, E., et al. 2005, A&A, 439, 863, doi: [10.1051/0004-6361:20041961](https://doi.org/10.1051/0004-6361:20041961)
- Insera, C., Sullivan, M., Angus, C. R., et al. 2021, MNRAS, 504, 2535, doi: [10.1093/mnras/stab978](https://doi.org/10.1093/mnras/stab978)
- Janiuk, A., Bejger, M., Charzyński, S., & Sukova, P. 2017, New Astronomy, 51, 7, doi: [10.1016/j.newast.2016.08.002](https://doi.org/10.1016/j.newast.2016.08.002)
- Kasen, D., Badnell, N. R., & Barnes, J. 2013, ApJ, 774, 25, doi: [10.1088/0004-637X/774/1/25](https://doi.org/10.1088/0004-637X/774/1/25)
- Kasliwal, M. M., Nakar, E., Singer, L. P., et al. 2017, Science, 358, 1559, doi: [10.1126/science.aap9455](https://doi.org/10.1126/science.aap9455)
- Kauffmann, G., Heckman, T. M., White, S. D. M., et al. 2003, MNRAS, 341, 54, doi: [10.1046/j.1365-8711.2003.06292.x](https://doi.org/10.1046/j.1365-8711.2003.06292.x)
- Kawaguchi, K., Shibata, M., & Tanaka, M. 2018, ApJL, 865, L21, doi: [10.3847/2041-8213/aade02](https://doi.org/10.3847/2041-8213/aade02)
- Kawanomoto, S., Uraguchi, F., Komiyama, Y., et al. 2018, PASJ, 70, 66, doi: [10.1093/pasj/psy056](https://doi.org/10.1093/pasj/psy056)
- Klingler, N. J., Lien, A., Oates, S. R., et al. 2021, The Astrophysical Journal, 907, 97, doi: [10.3847/1538-4357/abd2c3](https://doi.org/10.3847/1538-4357/abd2c3)

- Komiyama, Y., Obuchi, Y., Nakaya, H., et al. 2018, PASJ, 70, S2, doi: [10.1093/pasj/psx069](https://doi.org/10.1093/pasj/psx069)
- LIGO Scientific Collaboration, & Virgo Collaboration. 2020, GRB Coordinates Network, 27184, 1
- Lipunov, V. M., Gorbovskoy, E., Kornilov, V. G., et al. 2017, ApJL, 850, L1, doi: [10.3847/2041-8213/aa92c0](https://doi.org/10.3847/2041-8213/aa92c0)
- Martin, R. G., Nixon, C., Xie, F.-G., & King, A. 2018, MNRAS, 480, 4732, doi: [10.1093/mnras/sty2178](https://doi.org/10.1093/mnras/sty2178)
- McKernan, B., Ford, K. E. S., Bartos, I., et al. 2019, ApJL, 884, L50, doi: [10.3847/2041-8213/ab4886](https://doi.org/10.3847/2041-8213/ab4886)
- Metzger, B. D. 2019, Living Reviews in Relativity, 23, 1, doi: [10.1007/s41114-019-0024-0](https://doi.org/10.1007/s41114-019-0024-0)
- Miyazaki, S., Komiyama, Y., Nakaya, H., et al. 2012, in Society of Photo-Optical Instrumentation Engineers (SPIE) Conference Series, Vol. 8446, Ground-based and Airborne Instrumentation for Astronomy IV, ed. I. S. McLean, S. K. Ramsay, & H. Takami, 84460Z, doi: [10.1117/12.926844](https://doi.org/10.1117/12.926844)
- Miyazaki, S., Komiyama, Y., Kawanomoto, S., et al. 2018, PASJ, 70, S1, doi: [10.1093/pasj/psx063](https://doi.org/10.1093/pasj/psx063)
- Morgan, R., Palmese, A., Garcia, A., et al. 2020, GRB Coordinates Network, 27366, 1
- Moriya, T. J., Tanaka, M., Yasuda, N., et al. 2019, ApJS, 241, 16, doi: [10.3847/1538-4365/ab07c5](https://doi.org/10.3847/1538-4365/ab07c5)
- Morokuma, T., Tanaka, M., Asakura, Y., et al. 2016, PASJ, 68, L9, doi: [10.1093/pasj/psw061](https://doi.org/10.1093/pasj/psw061)
- Nicholl, M., Berger, E., Kasen, D., et al. 2017, ApJL, 848, L18, doi: [10.3847/2041-8213/aa9029](https://doi.org/10.3847/2041-8213/aa9029)
- Niino, Y., Totani, T., & Okumura, J. E. 2014, PASJ, 66, L9, doi: [10.1093/pasj/psu115](https://doi.org/10.1093/pasj/psu115)
- Nugent, P., Kim, A., & Perlmutter, S. 2002, PASP, 114, 803, doi: [10.1086/341707](https://doi.org/10.1086/341707)
- Oates, S. R., Marshall, F. E., Breeveld, A. A., et al. 2021, Monthly Notices of the Royal Astronomical Society, 507, 1296, doi: [10.1093/mnras/stab2189](https://doi.org/10.1093/mnras/stab2189)
- Oguri, M., & Marshall, P. J. 2010, MNRAS, 405, 2579, doi: [10.1111/j.1365-2966.2010.16639.x](https://doi.org/10.1111/j.1365-2966.2010.16639.x)
- Ohgami, T., Tominaga, N., Morokuma, T., et al. 2020, GRB Coordinates Network, 27205, 1
- Ohgami, T., Tominaga, N., Utsumi, Y., et al. 2021, PASJ, 73, 350, doi: [10.1093/pasj/psab002](https://doi.org/10.1093/pasj/psab002)
- Okumura, J. E., Ihara, Y., Doi, M., et al. 2014, PASJ, 66, 49, doi: [10.1093/pasj/psu024](https://doi.org/10.1093/pasj/psu024)
- Pei, Y. C. 1992, ApJ, 395, 130, doi: [10.1086/171637](https://doi.org/10.1086/171637)
- Perego, A., Radice, D., & Bernuzzi, S. 2017, ApJL, 850, L37, doi: [10.3847/2041-8213/aa9ab9](https://doi.org/10.3847/2041-8213/aa9ab9)
- Pian, E., D’Avanzo, P., Benetti, S., et al. 2017, Nature, 551, 67, doi: [10.1038/nature24298](https://doi.org/10.1038/nature24298)
- Planck Collaboration, Ade, P. A. R., Aghanim, N., et al. 2014, A&A, 571, A16, doi: [10.1051/0004-6361/201321591](https://doi.org/10.1051/0004-6361/201321591)
- Pratten, G., García-Quirós, C., Colleoni, M., et al. 2021, PhRvD, 103, 104056, doi: [10.1103/PhysRevD.103.104056](https://doi.org/10.1103/PhysRevD.103.104056)
- Quimby, R. M., Oguri, M., More, A., et al. 2014, Science, 344, 396, doi: [10.1126/science.1250903](https://doi.org/10.1126/science.1250903)
- Rosswog, S., Sollerman, J., Feindt, U., et al. 2018, A&A, 615, A132, doi: [10.1051/0004-6361/201732117](https://doi.org/10.1051/0004-6361/201732117)
- Sasada, M., Utsumi, Y., Itoh, R., et al. 2021, Progress of Theoretical and Experimental Physics, 2021, 05A104, doi: [10.1093/ptep/ptab007](https://doi.org/10.1093/ptep/ptab007)
- Schlaflly, E. F., & Finkbeiner, D. P. 2011, ApJ, 737, 103, doi: [10.1088/0004-637X/737/2/103](https://doi.org/10.1088/0004-637X/737/2/103)
- Shen, S., Mo, H. J., White, S. D. M., et al. 2003, MNRAS, 343, 978, doi: [10.1046/j.1365-8711.2003.06740.x](https://doi.org/10.1046/j.1365-8711.2003.06740.x)
- Shibata, M., Fujibayashi, S., Hotokezaka, K., et al. 2017, PhRvD, 96, 123012, doi: [10.1103/PhysRevD.96.123012](https://doi.org/10.1103/PhysRevD.96.123012)
- Singer, L. P., & Price, L. R. 2016, PhRvD, 93, 024013, doi: [10.1103/PhysRevD.93.024013](https://doi.org/10.1103/PhysRevD.93.024013)
- Smartt, S. J., Chen, T. W., Jerkstrand, A., et al. 2017, Nature, 551, 75, doi: [10.1038/nature24303](https://doi.org/10.1038/nature24303)
- Soares-Santos, M., Holz, D. E., Annis, J., et al. 2017, ApJL, 848, L16, doi: [10.3847/2041-8213/aa9059](https://doi.org/10.3847/2041-8213/aa9059)
- Tagawa, H., Haiman, Z., Bartos, I., & Kocsis, B. 2020a, ApJ, 899, 26, doi: [10.3847/1538-4357/aba2cc](https://doi.org/10.3847/1538-4357/aba2cc)
- Tagawa, H., Haiman, Z., & Kocsis, B. 2020b, ApJ, 898, 25, doi: [10.3847/1538-4357/ab9b8c](https://doi.org/10.3847/1538-4357/ab9b8c)
- Tanaka, M. 2016, Advances in Astronomy, 2016, 634197, doi: [10.1155/2016/6341974](https://doi.org/10.1155/2016/6341974)
- Tanaka, M., Utsumi, Y., Mazzali, P. A., et al. 2017, PASJ, 69, 102, doi: [10.1093/pasj/psx121](https://doi.org/10.1093/pasj/psx121)
- Tanvir, N. R., Levan, A. J., González-Fernández, C., et al. 2017, ApJL, 848, L27, doi: [10.3847/2041-8213/aa90b6](https://doi.org/10.3847/2041-8213/aa90b6)
- The LIGO Scientific Collaboration, the Virgo Collaboration, the KAGRA Collaboration, et al. 2021, arXiv e-prints, arXiv:2111.03606. <https://arxiv.org/abs/2111.03606>
- Tominaga, N., Tanaka, M., Morokuma, T., et al. 2018a, PASJ, 70, 28, doi: [10.1093/pasj/psy007](https://doi.org/10.1093/pasj/psy007)
- Tominaga, N., Niino, Y., Totani, T., et al. 2018b, PASJ, 70, 103, doi: [10.1093/pasj/psy101](https://doi.org/10.1093/pasj/psy101)
- Troja, E., Piro, L., van Eerten, H., et al. 2017, Nature, 551, 71, doi: [10.1038/nature24290](https://doi.org/10.1038/nature24290)
- Utsumi, Y., Tominaga, N., Tanaka, M., et al. 2017, PASJ, 70, 1, doi: [10.1093/pasj/psx125](https://doi.org/10.1093/pasj/psx125)
- Valenti, S., Sand, D. J., Yang, S., et al. 2017, ApJL, 848, L24, doi: [10.3847/2041-8213/aa8edf](https://doi.org/10.3847/2041-8213/aa8edf)
- Vanden Berk, D. E., Wilhite, B. C., Kron, R. G., et al. 2004, ApJ, 601, 692, doi: [10.1086/380563](https://doi.org/10.1086/380563)
- Yamazaki, R., Asano, K., & Ohira, Y. 2016, Progress of Theoretical and Experimental Physics, 2016, 051E01, doi: [10.1093/ptep/ptw042](https://doi.org/10.1093/ptep/ptw042)

York, D. G., Adelman, J., Anderson, John E., J., et al.
2000, AJ, 120, 1579, doi: [10.1086/301513](https://doi.org/10.1086/301513)